Research Square

Preprints are preliminary reports that have not undergone peer review.
They should not be considered conclusive, used to inform clinical practice,
or referenced by the media as validated information.

Statistical performance evaluation of hybrid RIS-assistedair-to-satellite terahertz communication systems withinatmospheric transmission windows

Mubark Alghamdi

msalgamdi@kku.edu.sa

King Khalid university

Ivica Kostanic

Florida Institute of Technology

Mohammed M.Alammar

King Khalid university

Research Article

Keywords: 6G wireless networks; air-to-satellite communications; atmospheric propagation; nonterrestrial networks; reconfigurable intelligent surface; spectral efficiency; terahertz communications

Posted Date: November 20th, 2026

DOI: https://doi.org/10.21203/rs.3.rs-11694011/v1

License: This work is licensed under a Creative Commons Attribution 4.0 International License.
Read Full License

Additional Declarations: No competing interests reported.

Statistical performance evaluation of hybrid RIS-assisted air-to-satellite terahertz communication systems within atmospheric transmission windows

Mubark Alghamdi[1*], Ivica Kostanic[2] and Mohammed M. Alammar[1]

[1]Department of Electrical Engineering, King Khalid University, Abha 61421, Saudi Arabia
[2]Department of Electrical Engineering and Computer Science, Florida Institute of Technology, Melbourne, FL 32901, USA

[*]Corresponding author: Mubark Alghamdi, msalgamdi@kku.edu.sa

Abstract

Terahertz links between high-altitude platforms and low-Earth-orbit satellites are candidates for sixth-generation non-terrestrial backhaul, but severe spreading loss, molecular absorption, and platform dynamics leave their practical operating envelope uncertain. Prior evaluations rely largely on ground-anchored absorption models and idealized geometry, so the joint influence of atmospheric, geometric, and hardware parameters at platform altitude remains insufficiently quantified. This study evaluates a physics-based link model that combines altitude-resolved ITU-R P.676/P.835 absorption, reflectarray aperture gain, stochastic pointing error, satellite pass dynamics, and phase-coherence, ephemeris, Doppler, and control-latency budgets over 5,000 simulated links spanning 100–420 GHz, platform altitudes of 8–18 km, orbits of 500–1200 km, and arrays of 2^{10} to 2^{18} elements, with standardized regression quantifying each parameter's influence. Array size is the strongest positive factor ($\beta = +0.734$) and carrier frequency the strongest negative one ($\beta = -0.319$); above roughly 8 km, window absorption falls below 0.2 dB and spreading loss dominates. Mean signal-to-noise ratio crosses 0 dB between 2^{15} and 2^{16} elements, corresponding to panels of 9–35 cm at 220 GHz. Alignment holds fully at 0.02° residual jitter, whereas 0.10° reduces the largest array's alignment to 48.7% and its mean spectral efficiency from 3.82 to 2.72 bps/Hz, and surface stability of 34–82 μm RMS bounds coherence loss at 1 dB. Aperture size and tracking accuracy must therefore be chosen jointly, and the quantified tolerances give concrete design guidance for reconfigurable-intelligent-surface-assisted terahertz air-to-satellite links.

Keywords: 6G wireless networks; air-to-satellite communications; atmospheric propagation; non-terrestrial networks; reconfigurable intelligent surface; spectral efficiency; terahertz communications

1 Introduction

The rapid evolution toward sixth-generation (6G) wireless communication systems is expected to transform global connectivity by supporting ultra-high data rates, ultra-low latency, massive device connectivity, and highly reliable communication services [1]. These capabilities are essential for enabling emerging applications such as extended reality, intelligent transportation, digital twins, and large-scale Internet of Things (IoT) networks, all of which require seamless and high-capacity wireless connectivity [2]. To meet these demanding requirements, the terahertz (THz) spectrum has attracted considerable attention because of its abundant bandwidth and potential to achieve terabit-per-second data transmission [3]. Meanwhile, future 6G networks are transitioning toward integrated space–air–ground architectures [4]. In this paradigm, air-to-satellite and non-terrestrial networks are expected to provide seamless coverage and ubiquitous connectivity. Consequently, THz-enabled air-to-satellite communications have emerged as a promising solution for realizing ubiquitous global wireless connectivity [5].

Despite these advantages, the practical deployment of THz air-to-satellite communication systems remains challenging due to the unique propagation characteristics of high-frequency electromagnetic waves [6]. THz signals experience severe free-space path loss that increases with both carrier frequency and transmission distance, while molecular absorption caused primarily by atmospheric oxygen and water vapor introduces significant frequency-dependent attenuation [7]. Additional atmospheric effects, including turbulence and environmental variability, further degrade signal quality and increase channel uncertainty [8]. The long transmission distances and continuously changing geometric conditions of air-to-satellite links compound these impairments, where platform altitude, satellite position, and elevation angle jointly influence propagation characteristics [9]. As a result, the signal-to-noise ratio (SNR) and achievable spectral efficiency are significantly constrained, emphasizing the need for communication strategies that effectively mitigate propagation losses under realistic atmospheric conditions [10].

Reconfigurable Intelligent Surfaces (RIS) have emerged as a promising technology for addressing these propagation challenges [11]. By employing programmable passive reflecting elements, RIS can intelligently manipulate electromagnetic wave propagation through passive beamforming, redirecting signals toward intended receivers without requiring active radio-frequency transmission [12]. This capability enhances the received signal strength, compensates for propagation losses, extends communication coverage, and improves both link reliability and spectral efficiency [13]. Owing to these advantages, RIS has become an important enabling technology for future THz communication systems and is increasingly considered a key component of integrated satellite and non-terrestrial wireless networks [14].

Recent research has substantially advanced the understanding of THz communication channels and RIS-assisted wireless systems [3]. Existing studies have established comprehensive propaga-

tion models incorporating free-space path loss, molecular absorption, atmospheric attenuation, and turbulence to characterize THz channel behavior under realistic environmental conditions [15]. Standardized propagation models, including ITU-R P.676 and ITU-R P.835, have been widely adopted to evaluate atmospheric propagation in THz communication systems. These models have shown that THz satellite communication is most feasible within low-attenuation atmospheric transmission windows, particularly around 140 and 220 GHz [9]. Furthermore, several studies have demonstrated that practical THz communication is feasible primarily within specific atmospheric transmission windows where molecular absorption is relatively low [7]. In parallel, extensive research has shown that RIS can effectively enhance communication performance by improving received signal power, extending coverage, mitigating propagation losses, and increasing spectral efficiency [16]. Furthermore, the integration of RIS into satellite and non-terrestrial communication networks has attracted growing attention as a promising approach for improving connectivity, coverage, and communication reliability in future 6G systems [14]. Although these studies have significantly advanced THz communication technologies, existing performance evaluations have predominantly focused on channel modeling, beamforming optimization, resource allocation, or communication performance enhancement using analytical and optimization-based approaches [17].

Despite these important contributions, there remains limited research that systematically quantifies the relative influence of multiple communication and propagation parameters on the performance of hybrid RIS-assisted air-to-satellite THz communication systems [18]. In particular, comprehensive statistical investigations that simultaneously evaluate the effects of carrier frequency, RIS configuration, transmission geometry, atmospheric attenuation, and transmit power on spectral efficiency within viable atmospheric transmission windows remain scarce [3]. Such analyses are essential for identifying the dominant factors governing communication performance and for establishing evidence-based design guidelines for future THz-enabled non-terrestrial communication systems [19].

Accordingly, this study systematically investigates the influence of communication, propagation, and geometric parameters on the spectral efficiency of hybrid RIS-assisted air-to-satellite THz communication systems operating within viable atmospheric transmission windows. A fully specified physics-based channel model (presented in complete, reproducible form in Section 3) is combined with comprehensive statistical analysis to quantify the relative effects of key system parameters on communication performance and to identify the principal determinants of spectral efficiency under realistic operating conditions. By providing a systematic evaluation of the relationships between atmospheric propagation, RIS provisioning, transmission geometry, and communication performance, this study offers practical insights that support the design of efficient, reliable, and propagation-aware RIS-assisted THz air-to-satellite communication systems for future non-terrestrial wireless networks. A further contribution is reproducibility: the complete channel model is stated in closed form with a worked link budget, and every dataset, table, and figure is regenerated from the govern-

ing equations by a single fixed-seed pipeline released as supplementary material, so that all reported numbers are traceable to the model without manual intervention.

2 Literature Review

2.1 THz Air-to-Satellite Communications and Atmospheric Channel Modeling

Terahertz (THz) communication is considered an enabling technology for sixth-generation (6G) wireless networks due to its high spectrum resources and ability to support ultra-high data-rate networks [3]. The propagation of reliable THz communication is, however, difficult due to the high sensitivity to free-space path loss, molecular absorption, atmospheric attenuation, and turbulence that affect the transmission of the communication signal over long distances [8]. These impairments are more prominent in the air-to-satellite scenario, where longer propagation paths and dynamic transmission geometry also affect the characteristics of the channel and system performance. For the accurate characterization of these propagation effects, widespread use of the ITU-R P.676 atmospheric gaseous attenuation model and the reference atmosphere model ITU-R P.835 has been adopted in THz communication research [9]. Using these standard models, Saqlain *et al.* [9] showed that THz communication between Earth and satellite is most viable in the atmospheric transmission windows with low attenuation, including 140 GHz and 220 GHz. Likewise, Chen *et al.* [20] demonstrated that molecular absorption, transmitting distance, and environmental conditions have a significant impact on network coverage and the number of transmission windows for THz communications. Da Nóbrega *et al.* [21] developed a channel-loss model by integrating molecular absorption and water-vapor continuum absorption, thus allowing for accurate channel prediction in the frequency range of 100–600 GHz and further improving propagation characterization. A few studies have also extended THz channel modeling to other non-terrestrial communication scenarios. In a recent paper, Kokkoniemi *et al.* [22] presented a more complete THz airplane-to-satellite channel model for frequency-selective propagation and Earth geometry that showed airborne THz links could reach capacities of up to 50–150 Gbps under favorable operating conditions. Nie and Akyildiz [23] studied inter-satellite THz link channels considering orbital perturbations and propagation effects, whereas Yang *et al.* [24] used ray-tracing techniques to analyze the time-varying characteristics of the links between space stations and satellites. All of these studies have helped to improve THz atmospheric channel modeling. However, the current literature mainly focuses on propagation characterization, propagation modeling, and channel-feasibility analysis, and the interplay of various propagation and communication parameters affecting system performance is not fully explored, especially in hybrid RIS-assisted air-to-satellite THz communication systems operating within feasible atmospheric transmission windows.

2.2 Reconfigurable Intelligent Surfaces for THz and Non-Terrestrial Communications

Reconfigurable Intelligent Surfaces (RIS) are a novel technology that can enhance the capabilities of future sixth-generation (6G) wireless communication systems [25]. In an RIS, passive beamforming is achieved by a programmable array of passive reflecting elements that intelligently manipulate the propagation of electromagnetic waves to boost signal strength, alleviate propagation loss, and increase the range of communication coverage without the need for active radio-frequency components [26]. Björnson and Sanguinetti [27] presented a thorough theoretical analysis of the fundamental propagation features and path loss of RIS-assisted communication systems, laying a solid theoretical foundation for the practical deployment of RIS. Recent works have shown that RIS can be used to solve the propagation issues of terahertz (THz) communications based on these concepts. In their review article, Othman *et al.* [25] presented the latest advancements in developing RIS-assisted THz systems, including advances in channel estimation, beamforming techniques, hardware architectures, and implementation challenges. In the same context, Ahmed *et al.* [28] pointed out that RIS can play a crucial role in enhancing the coverage and spectral efficiency of communication systems, and identified the research issues involved in future THz communication systems. Moreover, Zhao *et al.* [29] demonstrated significant spectral-efficiency gains by optimizing the reflected signals through passive beamforming, while Chen *et al.* [30] showed that RIS boosts communication performance and, at the same time, achieves energy-efficiency savings by lowering the power consumption of the transmitter. The use of RIS has also extended to satellite and non-terrestrial communication systems. Worka *et al.* [19] emphasized that RIS will play a significant role in future communications of satellite, high-altitude-platform, and unmanned-aerial-vehicle systems, enabling better coverage, communication reliability, and network efficiency in the context of integrated non-terrestrial networks. Moreover, Tariq *et al.* [31] examined the latest advancements in RIS-aided 6G communication systems, highlighting the practical implementation challenges and synergies between RIS and future THz communication technologies. While these studies show the immense potential of RIS for supporting THz and non-terrestrial communications, the majority of the existing literature concentrates only on beamforming optimization and communication improvement, and relatively less work has examined the impact of RIS configuration and atmospheric propagation on communication performance.

2.3 Performance Evaluation of RIS-Assisted THz Communication Systems

Performance evaluation is a pivotal aspect in assessing the reliability and effectiveness of RIS-assisted terahertz (THz) communication systems [32]. Analytical models, link-budget analysis, Monte Carlo simulations, and numerical simulations have been used to analyze communication performance in realistic propagation environments, as explored in existing studies [33]. These techniques take into

consideration the impact of atmospheric turbulence, pointing errors, non-ideal CSI, and propagation impairments, allowing for a comprehensive understanding of the behavior of RIS-assisted THz communication systems [34, 35]. The performance of communication systems is often measured by signal-to-noise ratio (SNR), spectral efficiency, channel capacity, outage probability, and bit error rate (BER) [36]. Hou and Li [37] studied the outage probability, channel capacity, diversity order, and SNR for RIS-assisted satellite communication systems with various RIS configurations. Likewise, an analytical BER expression was obtained and Monte Carlo simulations in Wang *et al.* [38] evaluated the effect of the number of RIS elements, zenith angle, receiver aperture, and SNR. Varotsos *et al.* [39] presented an analytical capacity model that takes into account free-space path loss, molecular absorption, atmospheric turbulence, and weather conditions, and Zhang *et al.* [40] proposed a practical space-air-ground integrated network channel model to calculate outage probability, ergodic rate, BER, and goodput in realistic propagation environments. Additionally, Nóbrega *et al.* [21] showed the impact of carrier frequency and atmospheric absorption on THz link performance by creating an improved propagation-loss model, while Tamesue *et al.* [34] conducted a link-budget and throughput analysis of THz feeder links under various weather conditions with the help of ITU-R atmospheric models. Moreover, Yuan *et al.* [35] studied the effect of atmospheric turbulence, pointing errors, RIS phase errors, and imperfect channel state information on the performance of RIS-assisted THz non-terrestrial networks. These studies have made significant progress in assessing RIS-assisted THz communication systems, but most of them focus on evaluating individual communication parameters or a particular optimization scenario. To the best of the authors' knowledge, the combined effect of communication, propagation, and geometric parameters on spectral efficiency under realistic atmospheric propagation conditions has not yet been systematically quantified. This limitation is the motivating factor for the present study, which carries out a thorough statistical analysis of air-to-satellite THz communication systems with a hybrid RIS to identify the key factors affecting communication performance.

2.4 Reconfigurable Surfaces and Non-Terrestrial Connectivity in Vehicular Technology

Parallel progress within the vehicular-technology community has framed reconfigurable surfaces and non-terrestrial links as core enablers of sixth-generation (6G) mobility and transportation services. In a survey of this area, Zhu *et al.* [41] consolidated the use of intelligent reflecting surfaces across ground-based and aerial vehicular scenarios and identified the blockage of millimeter-wave and THz signals as a primary motivation for surface-assisted propagation, which is precisely the impairment addressed by the RIS reflectarray considered in this study. From the aerial-platform perspective, Belmekki and Alouini [42] examined networked tethered flying platforms as persistent nodes within integrated non-terrestrial networks and detailed their channel models, coverage behavior, and backhaul roles, thereby motivating airborne feeds of the type assumed for the co-located active-passive

architecture adopted here. At the satellite tier, Almekhlafi *et al.* [43] analyzed low-earth-orbit coverage across several constellations and reported that elevation angle and satellite visibility strongly govern link quality in high-latitude regions, which reinforces the emphasis placed on transmission geometry as a determinant of spectral efficiency. These contributions establish the relevance of RIS-assisted non-terrestrial connectivity to future wireless networks; the joint statistical influence of carrier frequency, aperture provisioning, atmospheric absorption, and link geometry on air-to-satellite THz performance within viable transmission windows has, however, not yet been quantified, which is the gap addressed by the present study.

3 System Model and Physics-Based Channel Formulation

3.1 System Architecture

The considered link is illustrated in Fig. 1. It comprises three elements:

1. **Transmitter (TX).** An airborne platform (aircraft, UAV, or high-altitude platform) operating at altitude $h_p \in [8, 18]$ km, carrying an active terahertz feed with digital/analog beamforming.

2. **Reconfigurable intelligent surface (RIS).** A planar reflectarray of N passive phase-controllable elements, where N denotes the total number of RIS elements (unit cells) and $\lambda = c/f$ the carrier wavelength (c the speed of light, f the carrier frequency), at $\lambda/2$ pitch, *conformally mounted on the same airborne platform* and illuminated by the feed at a short standoff distance d_1 of a few metres.

3. **Receiver (RX).** A low-Earth-orbit satellite at altitude $h_s \in [500, 1200]$ km with a high-gain aperture antenna of gain G_r.

The term *hybrid* denotes the combination of *active* beamforming at the airborne feed with *passive* beamforming across the RIS aperture, in the sense used for hybrid RIS-empowered terahertz architectures [18]. The RIS is airborne and co-located with the transmitter; it is not ground-mounted and does not constitute an independent relay node. Because the feed's radiation is fully intercepted by the co-located surface, no geometrically distinct direct path to the satellite exists; the RIS-directed path is the sole modelled propagation path.

The RIS in this work is implemented as a reconfigurable reflectarray integrated with the airborne platform. Unlike conventional RIS-assisted systems that employ a remotely deployed reflecting surface to assist an existing communication link, the proposed architecture combines an active feed with a co-located passive reconfigurable reflectarray to form a single steerable transmitting aperture. The term "RIS" is used because the reflectarray consists of programmable, passive, phase-controlled elements that provide reconfigurable beamforming capability.

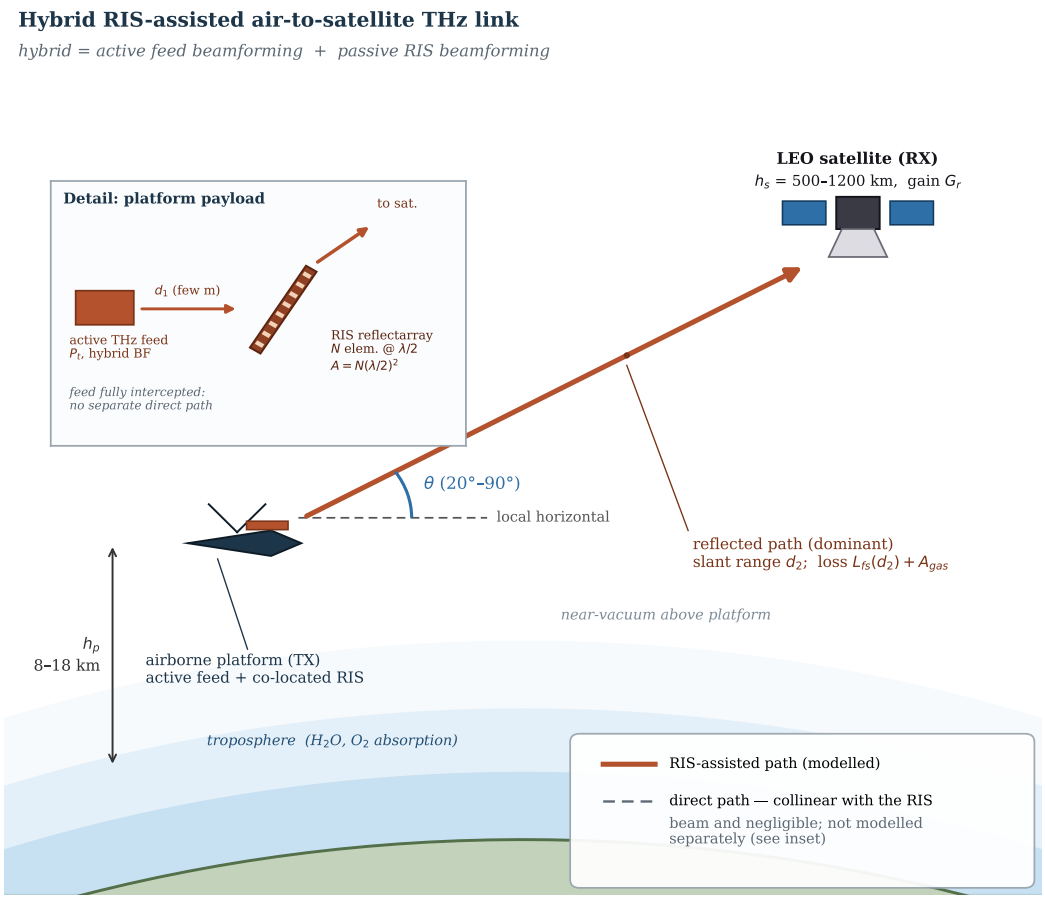


Figure 1: Hybrid RIS-assisted air-to-satellite terahertz link. An active terahertz feed on the airborne platform illuminates a co-located passive RIS reflectarray (detail inset), which phase-aligns the wavefront toward the LEO satellite over slant range d_2 at elevation angle θ.

3.2 Link Geometry

For a spherical Earth of radius $R_E = 6371\,\text{km}$, the slant range between the platform and the satellite at elevation angle θ is

$$d_2(\theta, h_p, h_s) = \sqrt{(R_E + h_s)^2 - \left[(R_E + h_p)\cos\theta\right]^2} - (R_E + h_p)\sin\theta. \tag{1}$$

Table 1: Zenith gaseous attenuation (dB) above platform altitude, by layered ITU-R P.676-12 integration over the ITU-R P.835 reference atmosphere.

f (GHz)	$h_p = 0$ km	8 km	12 km	16 km	18 km
140	1.65	0.04	0.01	0.00	0.00
183	78.08	4.51	0.93	0.14	0.05
220	4.31	0.06	0.01	0.00	0.00
325	97.53	4.82	1.08	0.22	0.09
340	15.94	0.19	0.02	0.00	0.00

3.3 Propagation Model

3.3.1 Free-space path loss

The free-space loss over the slant path follows the Friis formulation,

$$L_{fs}(d_2, f) = \left(\frac{4\pi f d_2}{c}\right)^2, \qquad L_{fs}^{\mathrm{dB}} = 20\log_{10}\left(\frac{4\pi f d_2}{c}\right), \tag{2}$$

with c the speed of light and f the carrier frequency.

3.3.2 Gaseous absorption

Molecular absorption is evaluated by layered integration of the ITU-R P.676-12 line-by-line specific attenuation $\gamma(f, P, T, \rho)$ over the ITU-R P.835 reference atmosphere, *starting at the platform altitude* h_p rather than at the surface:

$$A_{\mathrm{zen}}(f, h_p) = \int_{h_p}^{h_{\max}} \gamma\big(f, P(z), T(z), \rho(z)\big)\, \mathrm{d}z, \tag{3}$$

with $h_{\max} = 80$ km. The slant-path value follows the cosecant law, valid to within 1% for $\theta \geq 15°$:

$$A_{gas}(f, \theta, h_p) = \frac{A_{\mathrm{zen}}(f, h_p)}{\sin\theta}. \tag{4}$$

Evaluating (3) from h_p is essential: the overwhelming majority of atmospheric water vapour lies below 8 km, so zenith absorption at 220 GHz falls from 4.31 dB at the surface to below 0.1 dB for $h_p \geq 8$ km (Table 1; Fig. 2).

3.4 RIS Gain Model

Because the feed is co-located with the RIS, essentially all radiated power is intercepted by the surface, and the propagation is a *single dominant hop* from the RIS aperture to the satellite. The

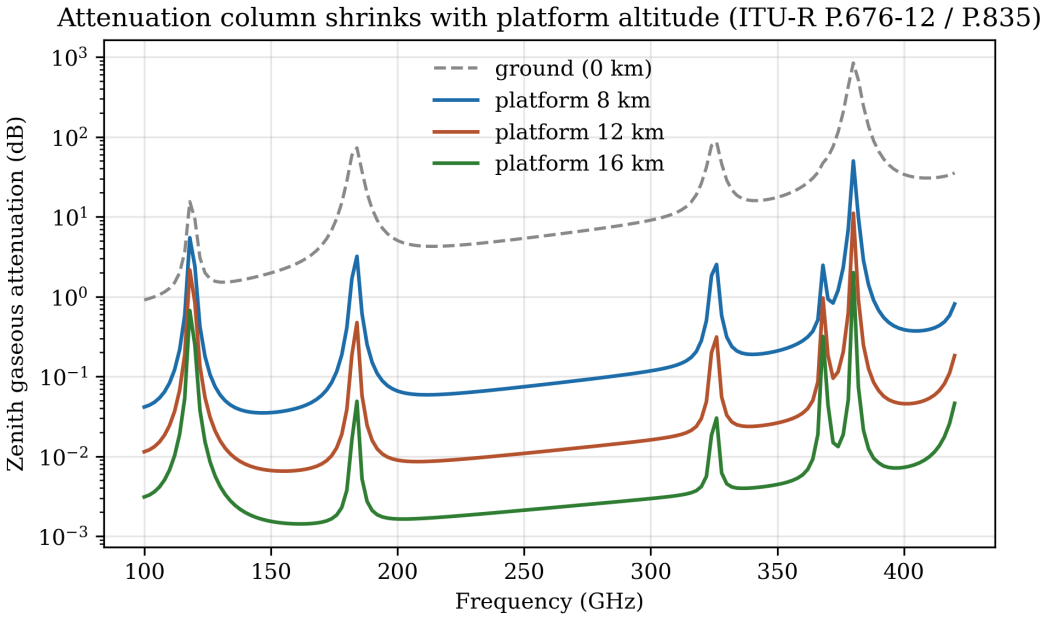


Figure 2: Zenith gaseous attenuation versus frequency for platform altitudes of 0, 8, 12, and 16 km (layered ITU-R P.676-12 over ITU-R P.835). The water-vapour absorption lines at 183 and 325 GHz, which dominate the ground-level spectrum, weaken by more than an order of magnitude at 8 km and by roughly two orders of magnitude at 12 km.

RIS therefore acts as a transmitting aperture of physical area

$$A_{\mathrm{RIS}} = N\left(\frac{\lambda}{2}\right)^{2}, \tag{5}$$

whose broadside gain under coherent phase alignment is

$$\begin{aligned} G_{\mathrm{RIS}} &= \frac{4\pi\eta_a A_{\mathrm{RIS}}}{\lambda^2} = \pi\eta_a N, \\ G_{\mathrm{RIS}}^{\mathrm{dB}} &= 10\log_{10}(\pi\eta_a N), \end{aligned} \tag{6}$$

where η_a is the aperture efficiency (taken as 0.6, accounting for spillover, taper, and discrete phase quantization).

Constant η_a and the near-field caveat. Holding η_a fixed across the full array-size range is a simplification that flatters the largest apertures, and its direction of bias should be stated. The feed-RIS standoff is fixed at a few metres while the aperture grows with N; the Fraunhofer distance $2D^2/\lambda$ of the surface at 220 GHz is only ≈ 0.7 m for $N = 2^{10}$ but rises to ≈ 45 m for $N = 2^{16}$ and ≈ 179 m for $N = 2^{18}$. The largest arrays are therefore illuminated well within their near field, where uniform coherent illumination is not automatic: the amplitude taper across the aperture steepens with N, so the true illumination efficiency should *decrease* with N rather than remain constant.

A constant $\eta_a = 0.6$ consequently over-states the effective gain of the largest arrays. The effect enters only as an additive $10\log_{10}\eta_a$ term: a drop to, say, $\eta_a = 0.4$ at $N = 2^{18}$ would subtract $\approx 1.8\,\mathrm{dB}$ from that array's gain, shifting its mean SNR by less than the 3.01 dB granted by a single doubling of N and leaving the qualitative ranking and the order-of-magnitude sizing rule intact. The quantitative sizing figures for the largest arrays should nonetheless be read as slightly optimistic on this account, and a full near-field illumination model is identified as future work.

Relation to the cascaded N^2 formulation. When the RIS is a *remote* relay, the link is a cascade of two independent far-field segments and the received power scales as $P_r \propto N^2/(d_1^2 d_2^2)$, yielding a $20\log_{10}(N)$ term [27]. The quadratic scaling arises because the surface both *captures* power in proportion to its area ($\propto N$) and *re-radiates* it directionally ($\propto N$). In the present co-located geometry the capture factor is already implicit in omitting $L_{fs}(d_1)$; counting it again would double the array contribution. Accordingly, (6) retains only the directivity term. This distinction is material: at $N = 1024$ the two formulations differ by 27.4 dB. For completeness, the remote-relay alternative was evaluated and found to place the received signal approximately 60 dB below the noise floor at the transmit powers considered; the co-located configuration is the only viable one at these frequencies and ranges.

3.5 Link Budget and SNR

Collecting the terms, the received power in decibels is

$$\begin{aligned} P_r^{\mathrm{dBW}} = P_t^{\mathrm{dBW}} + G_{\mathrm{RIS}}^{\mathrm{dB}} + G_r^{\mathrm{dB}} - L_{fs}^{\mathrm{dB}}(d_2, f) \\ - A_{gas}(f, \theta, h_p) - L_{\mathrm{ref}} - L_{\mathrm{point}} - L_{\mathrm{pol}}, \end{aligned} \tag{7}$$

where L_{ref} is the RIS element reflection loss ($|\Gamma| < 1$; 1 dB), L_{point} the beam pointing loss (1 dB), and L_{pol} the polarization mismatch (0.5 dB). The RIS is assumed to lie in the far field of the satellite, and the feed–RIS standoff is treated as an illumination efficiency folded into η_a rather than as a free-space segment.

Two idealizations in (7) should be made explicit, as they bear directly on the practicality of the large apertures identified later. First, L_{point} is modelled as a single fixed 1 dB penalty, whereas the half-power beamwidth of the coherent aperture narrows as N grows: at 220 GHz it is approximately 0.46° for $N = 2^{16}$ and 0.23° for $N = 2^{18}$. Holding a beam of a few tenths of a degree on a LEO satellite (orbital speed $\sim$7.5 km/s) from a moving airborne platform requires active closed-loop beam tracking, and the residual jitter of such a loop, not a static bias, is the operationally binding pointing term. A fixed 1 dB value is therefore optimistic for the largest arrays, and the SNR and spectral-efficiency figures reported for those arrays should be read as upper bounds in the pointing dimension. Second, THz front-end phase noise and hardware impairments, which are first-order

rather than second-order effects at these frequencies, are not represented; both are treated as out of scope here and identified as priorities in Section 3 limitations and the Conclusion.

Thermal noise power over bandwidth B with system noise temperature T_{sys} is

$$P_n^{\text{dBW}} = 10 \log_{10}(k_B T_{\text{sys}} B)\,, \tag{8}$$

with $k_B = 1.380649 \times 10^{-23}\,\text{J/K}$, giving

$$\text{SNR}^{\text{dB}} = P_r^{\text{dBW}} - P_n^{\text{dBW}}. \tag{9}$$

3.6 Spectral Efficiency and the Role of N

Spectral efficiency follows the Shannon expression

$$\begin{aligned} \eta_{SE} &= \log_2(1 + \text{SNR}) \quad [\text{bit/s/Hz}], \\ \text{SNR} &= 10^{\text{SNR}^{\text{dB}}/10}. \end{aligned} \tag{10}$$

The mechanism by which the RIS element count influences spectral efficiency is therefore an explicit chain:

$$\begin{aligned} N \xrightarrow{(5)} A_{\text{RIS}} \xrightarrow{(6)} G_{\text{RIS}} \\ \xrightarrow{(7),(9)} \text{SNR} \xrightarrow{(10)} \eta_{SE}. \end{aligned} \tag{11}$$

Adding elements enlarges the coherently phased aperture, which raises directive gain and hence received power and SNR; spectral efficiency then follows through the Shannon relation. Quantitatively, doubling N adds $10 \log_{10} 2 = 3.01\,\text{dB}$ of gain. In the high-SNR regime this yields approximately one additional bit/s/Hz per doubling, whereas near or below $\text{SNR} = 0\,\text{dB}$ the gain translates only sub-linearly, since $\log_2(1 + x) \approx x / \ln 2$ for small x. The RIS therefore exhibits diminishing returns precisely in the strongly attenuated configurations where it is most needed.

3.7 Worked Link-Budget Example

Table 2 evaluates (1)-(10) for a representative operating point: $f = 220\,\text{GHz}$, $h_p = 16\,\text{km}$, $h_s = 800\,\text{km}$, $\theta = 45°$, $N = 1024$, $\eta_a = 0.6$, $P_t = 30\,\text{dBm}$, $G_r = 54.6\,\text{dBi}$, $B = 1\,\text{GHz}$, $T_{\text{sys}} = 500\,\text{K}$. The receiver gain G_r, bandwidth B, and system noise temperature T_{sys} are held fixed throughout and should be read as assumptions rather than swept variables. Of these, $T_{\text{sys}} = 500\,\text{K}$ is optimistic for an uncooled THz front end; because noise enters (9) additively as $10 \log_{10} T_{\text{sys}}$, a more conservative $1000\,\text{K}$ would lower every SNR value by $3.0\,\text{dB}$, equivalent to removing one doubling of N, and would shift the viability transition upward by one array size (from between 2^{15} and 2^{16} to between

Table 2: Worked link budget at the representative operating point ($f = 220\,\mathrm{GHz}$, $h_p = 16\,\mathrm{km}$, $h_s = 800\,\mathrm{km}$, $\theta = 45°$, $N = 1024$).

Quantity	Value
Wavelength λ	$1.3627\,\mathrm{mm}$
RIS aperture $A_{\mathrm{RIS}} = N(\lambda/2)^2$	$4.75\,\mathrm{cm}^2$ ($2.18\,\mathrm{cm}$ square)
Slant range d_2	$1053.8\,\mathrm{km}$
Transmit power P_t	$+0.00\,\mathrm{dBW}$
RIS aperture gain G_{RIS}	$+32.86\,\mathrm{dBi}$
Satellite antenna gain G_r	$+54.60\,\mathrm{dBi}$
Free-space path loss L_{fs}	$-199.75\,\mathrm{dB}$
Gaseous absorption A_{gas}	$-0.00\,\mathrm{dB}$
Reflection loss L_{ref}	$-1.00\,\mathrm{dB}$
Pointing loss L_{point}	$-1.00\,\mathrm{dB}$
Polarization mismatch L_{pol}	$-0.50\,\mathrm{dB}$
Received power P_r	$-114.80\,\mathrm{dBW}$
Noise power P_n	$-111.61\,\mathrm{dBW}$
SNR	$\mathbf{-3.19\,dB}$
Spectral efficiency η_{SE}	$\mathbf{0.566\,bit/s/Hz}$

2^{16} and 2^{17}) without altering the ranking or the mechanism. The sizing figures below are stated at 500 K and scale by this simple one-doubling-per-3 dB rule for other noise assumptions.

3.8 Platform-Motion and Pointing-Error Model

The fixed 1 dB pointing penalty in (7) idealizes a tracking loop with negligible residual error. To quantify link stability under platform motion, the pointing loss is replaced for the stability analysis by a stochastic model. The half-power beamwidth of the coherently phased aperture is

$$\theta_{3\mathrm{dB}} \approx \frac{1.02\,\lambda}{D} = \frac{2.04}{\sqrt{N}}\ \mathrm{rad}, \qquad D = \sqrt{N}\,\frac{\lambda}{2}, \tag{12}$$

which depends only on N (0.46° at $N = 2^{16}$, 0.23° at $N = 2^{18}$). The residual boresight error θ_e after closed-loop tracking is modelled as Rayleigh distributed, $\theta_e \sim \text{Rayleigh}(\sigma)$, arising from independent zero-mean Gaussian jitter of standard deviation σ on each axis, the standard treatment of mispointing on narrow-beam links. Position fluctuations are negligible by comparison: a metre-scale displacement subtends under 10^{-4} degrees at 10^3 km range and changes free-space loss by under 10^{-5} dB, so attitude dominates. Because the feed–reflectarray pair is body-fixed, an attitude error maps into a net beam error of between one and two times its value depending on reflection geometry; σ is defined on the resulting boresight error, absorbing this factor. The instantaneous pointing loss follows the quadratic main-lobe approximation,

$$L_{\text{point}}(\theta_e) = \min\Big[12\big(\theta_e/\theta_{3\text{dB}}\big)^2,\, 30\Big] \text{ dB}, \tag{13}$$

capped at 30 dB to represent the sidelobe floor. Because turbulence and airframe vibration are platform- and scenario-dependent, σ is swept over $\{0.01, 0.02, 0.05, 0.10\}^\circ$ (0.17–1.75 mrad), spanning the sub-beamwidth tracking regime the apertures considered require; $\sigma = 0$ recovers the ideal-pointing baseline. One draw of θ_e is applied to each ensemble link per σ under the fixed seed. Alignment is defined as $L_{\text{point}} \le 3$ dB, i.e. $\theta_e \le \theta_{3\text{dB}}/2$, with closed form $\Pr[\text{align}] = 1 - \exp\big(-\theta_{3\text{dB}}^2/8\sigma^2\big)$.

3.9 LEO Pass Dynamics and Beam-Update Requirement

The ensemble of Section 3.11 samples static geometric snapshots. To characterize the dynamic channel over an actual satellite transit, a circular-orbit pass is propagated over the spherical-Earth geometry of (1): for $h_s = 800$ km and $h_p = 16$ km, the orbital velocity is 7.46 km/s and the line-of-sight angular rate seen from the platform peaks at 0.544°/s for an overhead pass and 0.160°/s for a 45°-maximum-elevation pass. Holding the beam within $\theta_{3\text{dB}}/10$ of boresight for the largest array ($N = 2^{18}$) therefore requires phase-profile updates at only $\approx$24 Hz (overhead) or $\approx$7 Hz (45° pass). Demonstrated RIS hardware reconfigures far faster: PIN- and varactor-based prototypes with 256–2430 elements switch states on microsecond-to-millisecond scales at total control powers near 1 W [44–46]. Platform attitude dynamics, not orbital motion, set the demanding case: body rates under manoeuvre, gusts, or turbulence can exceed the orbital term by one to two orders of magnitude, and holding $\theta_{3\text{dB}}/10$ at $N = 2^{18}$ against a 50°/s transient requires full-array phase updates near 2.2 kHz, with vibration rejection demanding correction bandwidths of several times the dominant airframe modes (tens to hundreds of Hz). PIN-switched elements change state on nanosecond-to-microsecond scales and demonstrated surfaces refresh their full phase profile at kilohertz-class rates [44, 45], so a margin of one to three orders of magnitude remains even in this regime. Electronic reconfiguration speed is thus not the binding constraint; the demanding element is the attitude-estimation and tracking loop, whose residual jitter determines link stability; this loop includes channel-estimation latency and accuracy, which the co-located geometry removes from the critical path, since beam

pointing is computed open-loop from inertial attitude and satellite ephemeris rather than from estimated channel state, leaving estimation residuals folded into σ, the quantity that Section 3.8 parameterizes. Azimuth sweeps by up to $\sim$180° across a near-overhead pass; boresight slewing of the platform-mounted aperture is assumed to absorb this, with any residual scan loss folded into the aperture efficiency and pointing terms, an idealization stated as such. Doppler over the pass is bounded by $fv/c \leq 5.6\,\mathrm{MHz}$ at 220 GHz and is assumed pre-compensated, as is standard for non-terrestrial links.

3.10 Phase Coherence, Ephemeris, Doppler, and Control-Latency Budgets

Beam pointing is not the only mechanism by which platform dynamics can degrade a coherent terahertz aperture, so the remaining mechanisms are budgeted here. Platform motion decomposes into three parts with distinct effects. Rigid-body translation changes the path length common to every element; at 300 GHz a 0.25 mm displacement shifts the carrier phase by 90°, but a common phase shift leaves the beamforming gain untouched and is absorbed by receiver carrier recovery in the same way as Doppler. Rigid-body rotation is the pointing error of Section 3.8. Structural deformation of the panel is the component that attacks coherence itself: a random surface error of RMS amplitude δ perturbs the two-way element phases by $\sigma_\phi = 4\pi\delta/\lambda$, reducing the coherent gain by the Ruze factor $\exp(-\sigma_\phi^2)$,

$$\Delta G_{\mathrm{Ruze}} = \frac{10\,\sigma_\phi^2}{\ln 10} = \frac{10}{\ln 10}\left(\frac{4\pi\delta}{\lambda}\right)^2 \ \mathrm{dB}. \tag{14}$$

Holding the loss below 1 dB requires $\delta \leq 82$, 52, and 34 μm RMS at 140, 220, and 340 GHz respectively. These tolerances are within established reflectarray practice: flight-qualified panels are fabricated to surface accuracies of tens of micrometres [47], so deformation is a structural design requirement rather than an obstacle, although gust and vibration response of a specific airframe must be verified against it.

Ephemeris quality sets a deterministic pointing bias of $\Delta p/d_2$ for transverse position error Δp. At the reference range of 1054 km, kilometre-class two-line-element ephemerides give a 0.054° bias, comparable to half the $N = 2^{18}$ beamwidth, whereas GNSS-grade knowledge (10 m) gives 0.0005°, which is negligible. Precise orbit data is therefore required before the largest arrays pay off; Section 4.9 quantifies the cost of ignoring this.

Doppler is bounded and smooth. Over the overhead reference pass the shift at 300 GHz reaches 6.24 MHz with a maximum rate of 63.2 kHz/s (6.51 MHz and 89.8 kHz/s for a 600 km orbit at 7.56 km/s), both orders of magnitude inside the pull-in range and tracking bandwidth of standard carrier-recovery loops; ephemeris-based pre-compensation with velocity knowledge of 0.1 m/s leaves a residual of only 100 Hz at 300 GHz. The complete control chain consists of state acquisition,

feedback, phase-profile computation, and RIS reconfiguration, and each stage is bounded. Acquisition is inertial attitude sensing at kilohertz rates with millisecond latency, fused with propagated ephemerides; because pointing is computed open-loop from these quantities rather than from estimated channel state, no over-the-air CSI feedback leg exists, and the feedback path is internal to the platform avionics. The phase profile follows from a closed-form steering vector in $O(N)$ operations with no iterative optimization, and reconfiguration itself is the microsecond-to-millisecond capability of Section 3.9 [44, 45]. An end-to-end latency below 20 ms is therefore attainable with current hardware, and channel-state acquisition stays off the tracking-critical path, so control latency T enters as a staleness pointing error ωT at line-of-sight rate ω: at the peak orbital rate of 0.544°/s, $T = 20$ ms contributes 0.011°, below the benign jitter level, while a 50°/s body-rate transient at the same latency would contribute 1° and must instead be handled by the kilohertz-class update capability established in Section 3.9.

3.11 Simulation Design

The dataset comprises 5,000 independent air-to-satellite communication links generated from the model of Sections 3.2–3.6. For each realization, the carrier frequency (100–420 GHz), elevation angle (20–90°), platform altitude (8–18 km), satellite altitude (500–1200 km), RIS array size ($N = 2^{10}$–2^{18}, i.e. 1,024–262,144 elements), and transmit power (10–30 dBm) were sampled independently; the bandwidth was fixed at 1 GHz and the satellite antenna gain at 54.6 dBi. The sampled ranges span 24 dB of aperture gain (across the nine array sizes) and 20 dB of transmit power; because standardized regression coefficients scale with the standard deviation of each predictor, the magnitudes and hence the ranking reported in Section 4 are properties of these chosen ranges, not of the physics in isolation. Widening the transmit-power range or narrowing the array-size range would move the two toward parity, and the ranking should be read accordingly. Link viability was assessed per realization as slant-path gaseous absorption not exceeding 10 dB at the sampled frequency, platform altitude, and elevation angle; 99.6% of sampled links satisfy this altitude-aware criterion. That the screen removes almost nothing is not incidental but is itself a consequence of the altitude-resolved model: once the platform is above 8 km the absorption lines have collapsed (Fig. 2), so the criterion excludes only the handful of realizations that fall on the narrow 183 and 325 GHz line cores at the lowest sampled altitudes. It is retained for transparency and to exclude those residual cores rather than as a selective feasibility screen.

Because the mapping from parameters to spectral efficiency contains no stochastic term, each realization is a *static geometric snapshot*: satellite altitude and elevation angle are sampled independently, with no orbital trajectory, relative velocity, or azimuth variation attached to individual draws (pass-level dynamics are treated separately in Section 3.9), and the ensemble constitutes a designed sensitivity experiment over the operating envelope rather than a random sample from a population. The regression in Section 4 is therefore best understood as an *analytic sensitivity decomposition*:

for a budget that is linear in the decibel-domain terms, the standardized coefficients estimate the range-weighted partial derivatives of SNR with respect to each design variable, and could in principle be obtained by differentiating (7) directly. What the regression adds is not statistical discovery but a single, commensurable ranking of these sensitivities on a common (standardized) scale, together with an explicit account of the two non-linear terms-the cosecant slant-range factor and the geometry of (1)-whose curvature makes the partial derivatives configuration-dependent and is what produces the mild residual heteroscedasticity and heavy tails reported below. Reported significance levels index sensitivity within the design space, not population inference, and the diagnostic tests (Durbin-Watson, Breusch-Pagan, Jarque-Bera) are included only to characterise the residual structure of the linear approximation, not as hypothesis tests about a data-generating population. For the regression, all predictors were standardized prior to estimation, and heteroscedasticity-consistent (HC3) standard errors were employed. Primary inference is conducted with SNR in decibels as the dependent variable, which is unbounded and avoids the censoring induced by the spectral-efficiency floor at zero; a companion model for spectral efficiency is reported for continuity. All results are generated by a fixed-seed pipeline supplied as supplementary material, which regenerates the dataset, every table, and every figure without manual intervention.

4 Results

4.1 Descriptive Statistics

Table 3 reports the central tendency and dispersion of the principal variables over the 4,981 viable links. Under the altitude-resolved absorption model, gaseous attenuation is small throughout the operating envelope (mean 0.14 dB, maximum 9.84 dB): once the platform is above 8 km, the water-vapour column that dominates ground-level THz attenuation lies almost entirely below the transmitter. SNR spans -30.6 to $+29.4$ dB with a mean of -1.76 dB, placing the ensemble squarely across the viability transition, and spectral efficiency ranges up to 9.75 bps/Hz.

4.2 Spectral Efficiency Across the Band

Figure 3 plots spectral efficiency against carrier frequency. Spectral efficiency declines across the band as frequency rises; under the altitude-resolved model this decline is attributable almost entirely to the growth of free-space path loss, since residual gaseous absorption above the platform is negligible outside the narrow line cores at 183 and 325 GHz. This contrasts with ground-anchored links, for which water-vapour absorption is a first-order constraint on window selection.

Table 3: Descriptive statistics for key channel variables.

Variable	M	SD	Min	Max
Frequency (GHz)	258.13	92.20	100.17	419.92
Elevation angle (deg)	54.90	20.15	20.02	90.00
Platform altitude (km)	13.03	2.86	8.00	18.00
Satellite altitude (km)	852.74	204.13	500.01	1199.69
Slant range (km)	1101.58	379.86	489.60	2420.96
Gaseous attenuation (dB)	0.14	0.59	0.00	9.84
RIS aperture gain (dBi)	45.11	7.86	32.86	56.94
SNR (dB)	−1.76	10.70	−30.58	29.36
Spectral efficiency (bps/Hz)	1.49	1.74	0.00	9.75

Note. $N = 4981$ viable links (99.6% of 5,000 sampled). SNR = signal-to-noise ratio; RIS = reconfigurable intelligent surface. Viability: slant-path gaseous absorption ≤ 10 dB at the sampled frequency, platform altitude, and elevation angle.

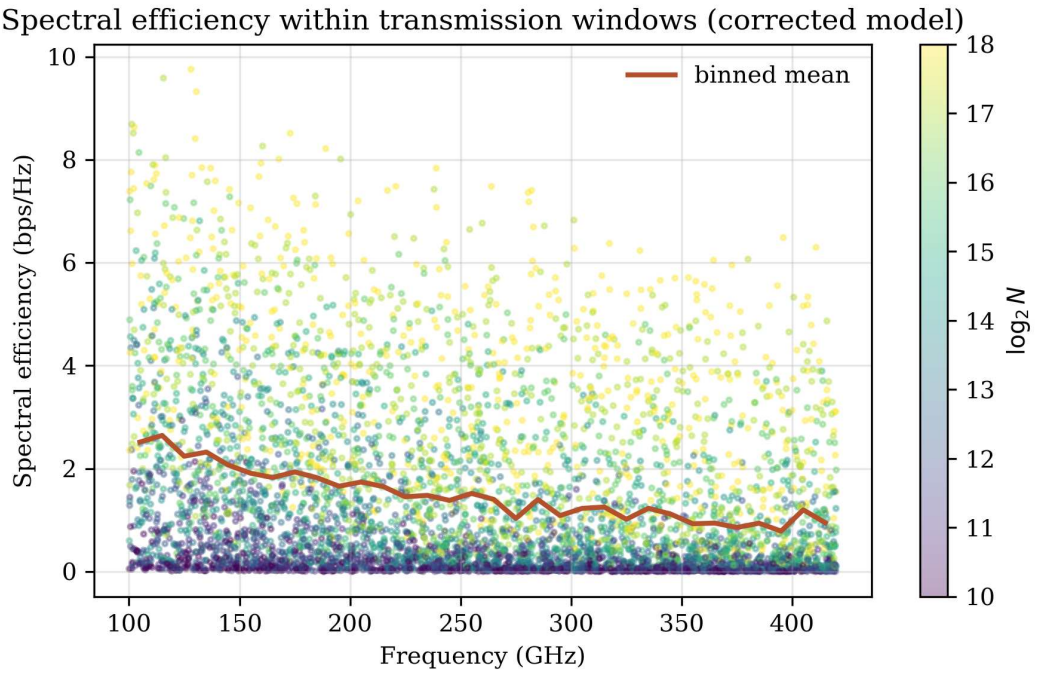


Figure 3: Spectral efficiency versus carrier frequency for the 4,981 viable links, coloured by RIS array size ($\log_2 N$). The red line is the binned mean. The downward trend reflects free-space spreading; the vertical stratification reflects the 3 dB-per-doubling aperture gain.

Table 4: Spectral efficiency by RIS array size.

RIS elements N	n	Gain (dBi)	Mean SNR (dB)	M (SE)	SD (SE)
1,024	554	32.86	−13.91	0.162	0.272
2,048	553	35.87	−11.26	0.264	0.397
4,096	523	38.88	−7.92	0.491	0.663
8,192	520	41.89	−4.73	0.801	0.953
16,384	563	44.90	−1.59	1.186	1.205
32,768	524	47.91	+1.44	1.659	1.408
65,536	535	50.92	+3.73	2.146	1.702
131,072	638	53.93	+6.96	2.854	1.835
262,144	571	56.94	+9.56	3.542	2.005

Note. SE = spectral efficiency (bps/Hz). Gain is the RIS aperture gain, $10\log_{10}(\pi\eta_a N)$ with $\eta_a = 0.6$. Kruskal-Wallis $H = 2658.9$, $p < .001$.

4.3 Effect of RIS Array Size

RIS array size raises the aperture gain by $10\log_{10}(\pi\eta_a N)$ dB (3.01 dB per doubling of N) and produces a monotonic spectral-efficiency improvement (Table 4, Fig. 4). Mean spectral efficiency rises from 0.162 bps/Hz at $N = 2^{10}$ to 3.542 bps/Hz at $N = 2^{18}$, with mean SNR crossing zero between $N = 2^{15}$ and $N = 2^{16}$ (32,768-65,536 elements). At 220 GHz these array sizes correspond to physical panels of only approximately 12-17 cm per side, and even $N = 2^{18}$ requires only a 35 cm panel, so the required apertures remain compatible with airborne platform integration. A Kruskal-Wallis test confirms that spectral efficiency differs across array sizes ($H = 2658.9$, $p < .001$).

4.4 Elevation and Geometry

Higher elevation angles shorten the slant range and thereby reduce free-space path loss, raising mean spectral efficiency (Fig. 5). Under the altitude-resolved absorption model, the elevation effect operates principally through geometry (slant range) rather than through cumulative atmospheric attenuation, since the absorbing column above the platform is thin; elevation and slant range are the geometric counterparts captured jointly in the regression ($r = -.68$ between them).

4.5 Correlations

Table 5 reports the Pearson correlation matrix; Fig. 6 visualizes the correlation of each design variable with the two performance outcomes. Spectral efficiency correlates positively with RIS array size ($r = .64$) and transmit power ($r = .50$), and negatively with frequency ($r = -.27$) and

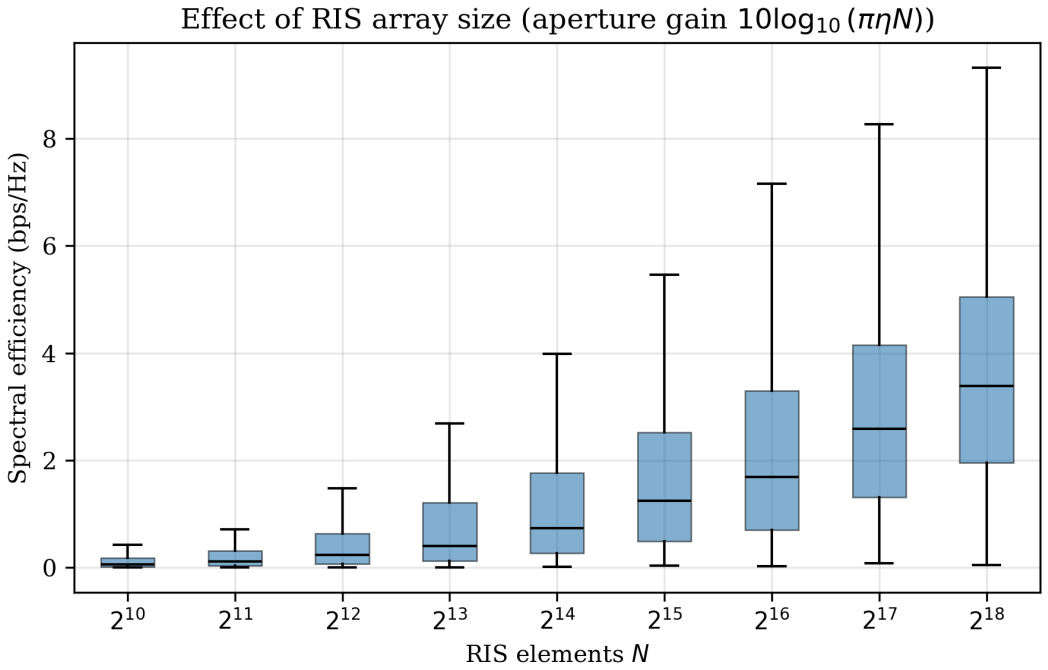


Figure 4: Spectral efficiency by RIS array size ($N = 2^{10}$–2^{18}). Box plots show medians, interquartile ranges, and 1.5×IQR whiskers; outliers omitted. The monotonic improvement follows the 3.01 dB-per-doubling aperture gain.

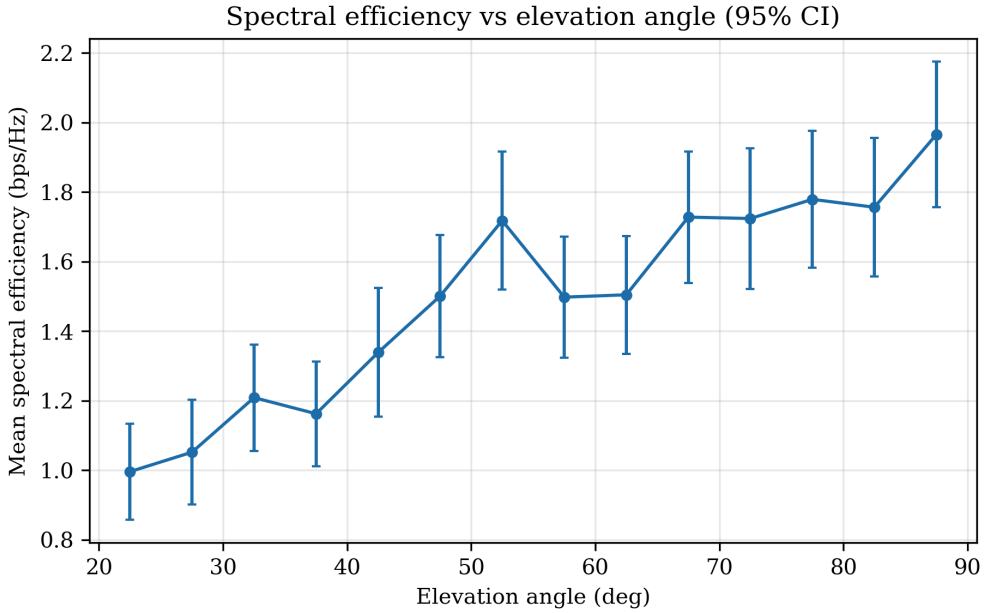


Figure 5: Mean spectral efficiency versus link elevation angle (5° bins; error bars denote 95% confidence intervals).

slant range ($r = -.23$). The correlation between gaseous attenuation and SNR is small ($r = -.08$):

Table 5: Pearson correlations among channel variables.

	1	2	3	4	5	6	7	8	9
1. Frequency	–								
2. Elevation	.02	–							
3. Slant range	−.01	−.68	–						
4. Platform alt.	.02	.01	−.02	–					
5. Gaseous atten.	.08	−.06	.05	−.18	–				
6. $\log_2 N$	.03	−.00	.02	−.02	.01	–			
7. Tx power	−.01	.01	−.01	−.02	−.01	.01	–		
8. SNR	−.30	.18	−.25	−.02	−.08	.72	.55	–	
9. Spectral eff.	−.27	.16	−.23	−.02	−.05	.64	.50	.90	–

Note. $N = 4981$. Leading zeros omitted per APA convention. Rows 8-9 involve definitional dependencies (see text).

in contrast to ground-anchored THz links, absorption above a high-altitude platform is too small to be a first-order driver of performance, and the frequency effect is carried almost entirely by free-space spreading. The correlations of spectral efficiency with SNR ($r = .90$) and of RIS gain with SNR are definitional consequences of Eqs. (7) and (10) and are reported for completeness rather than interpreted as findings. Because the design variables were sampled independently, their mutual correlations are zero to sampling precision (Table 5, rows 1–7), the sole exception being the elevation-slant-range pair ($r = -.68$), which is geometric rather than statistical. The correlations of the design variables with the two outcomes therefore recover, up to the effect of that single geometric coupling, the same information as the standardized regression of Section 4.6; this subsection and Fig. 6 are retained as a compact visual summary rather than as an independent analysis.

4.6 Regression and Diagnostics

Primary inference uses a standardized OLS regression of SNR (in dB) on six design parameters with HC3 heteroscedasticity-robust standard errors (Table 6). Consistent with the sensitivity-decomposition reading of Section 3.11, the coefficients are the range-weighted partial sensitivities of SNR to each design variable, and the near-unity fit ($R^2 = 0.992$) simply confirms that a linear-in-decibels model reproduces a budget that is itself linear apart from the cosecant and slant-range terms; R^2 is thus a measure of the fidelity of the linear approximation, not of explained population variance. RIS array size is the strongest predictor ($\beta = +0.734$), followed by transmit power ($\beta = +0.538$), carrier frequency ($\beta = -0.319$), and slant range ($\beta = -0.272$). Platform altitude carries a small but reliably positive coefficient ($\beta = +0.011$, $p < .001$), reflecting the residual absorption above lower platforms; elevation angle's marginal contribution is absorbed by slant range, its geometric counterpart. A companion model with spectral efficiency as the dependent variable ($R^2 = 0.793$) preserves the same ordering (RIS +0.646, power +0.493, frequency −0.288, slant range −0.246) and is provided for continuity with the Shannon-scale outcome.

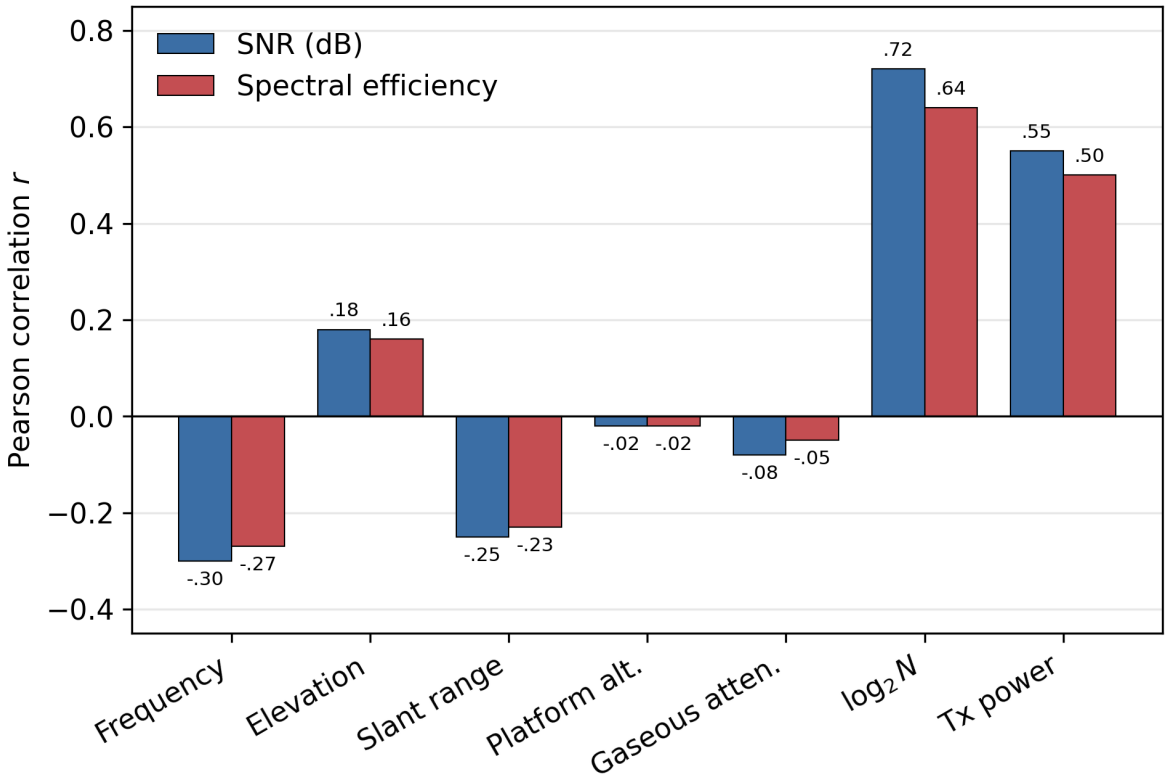


Figure 6: Pearson correlation of each channel variable with SNR and with spectral efficiency, taken from the correlation matrix of Table 5. RIS array size ($\log_2 N$) and transmit power are the dominant positive factors, while carrier frequency and slant range are the dominant negative factors.

Table 6: Standardized OLS regression (HC3 robust). Primary model: SNR (dB); companion model: spectral efficiency.

	Primary: SNR (dB)				Companion: SE			
Predictor	β	SE	t	p	β	SE	t	p
Frequency	−0.319	0.002	−204.8	$< .001$	−0.288	0.007	−41.2	$< .001$
Elevation angle	+0.002	0.002	1.3	.195	−0.004	0.008	−0.5	.624
RIS elements ($\log_2$)	+0.734	0.001	579.5	$< .001$	+0.646	0.008	85.1	$< .001$
Platform altitude	+0.011	0.001	8.7	$< .001$	+0.007	0.007	1.1	.262
Slant range	−0.272	0.002	−130.5	$< .001$	−0.246	0.009	−27.2	$< .001$
Transmit power	+0.538	0.001	421.8	$< .001$	+0.493	0.007	67.2	$< .001$
R^2			0.992				0.793	

Note. $N = 4981$. β = standardized coefficient; HC3 robust standard errors. Maximum VIF = 1.86 (elevation/slant range); all other VIF = 1.00. Given the deterministic design (Section 3.11), p-values index sensitivity within the design space rather than population inference.

Regression diagnostics (Table 7) confirm that both models are well conditioned: all variance inflation factors are below 2, the condition number is 2.3, and the Durbin-Watson statistics are

Table 7: Regression diagnostic tests.

Test	Primary (SNR)	Companion (SE)
Durbin-Watson (independence)	1.989	2.019
Breusch-Pagan (homoscedasticity)	$\chi^2 = 25.8$, $p < .001$	$\chi^2 = 43.2$, $p < .001$
Jarque–Bera (normality)	$\chi^2 = 16266$, $p < .001$	$\chi^2 = 1544$, $p < .001$
Maximum VIF	1.86	1.86
Condition number	2.3	2.3

Note. HC3 heteroscedasticity-consistent covariance used in both models. VIF < 5 and condition number < 30 indicate acceptable collinearity.

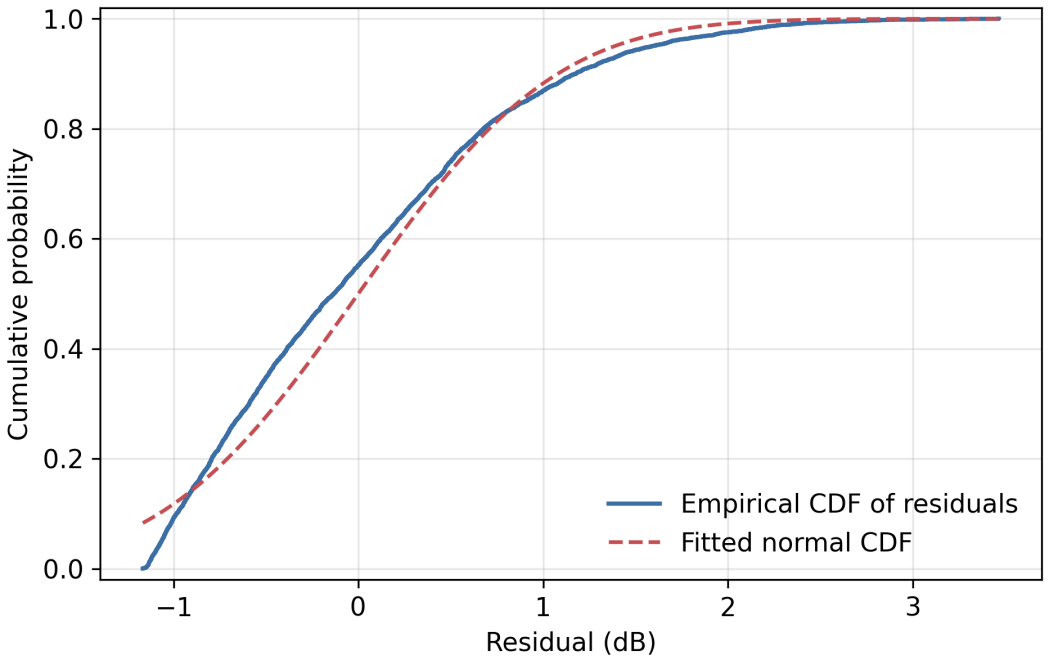


Figure 7: Empirical cumulative distribution of the primary (SNR-scale) model residuals (solid) against a fitted normal distribution (dashed). The residuals follow the normal reference near the centre and depart in the tails, so inference relies on HC3 robust standard errors.

near 2. Residuals of the primary model show mild heteroscedasticity and heavy tails, arising from the nonlinearities of the cosecant and slant-range terms; HC3 robust standard errors are therefore retained. Notably, the censoring artifact present when regressing spectral efficiency directly, a sharp lower boundary induced by the floor at zero, is absent on the SNR scale: the SNR-model residuals form a smooth distribution that follows the normal reference near the centre and departs only in the tails (Fig. 7). This is the principal methodological reason for conducting primary inference on SNR.

Table 8: Link stability versus per-axis pointing jitter σ: ensemble-mean spectral efficiency, alignment probability ($L_{\text{point}} \leq 3\,\text{dB}$), and outage ($\eta_{SE} < 3\,\text{bps/Hz}$).

σ	N	Mean SE	Align. (%)	Outage (%)
0 (ideal)	2^{18}	3.817	100.0	38.5
0.01°	2^{18}	3.804	100.0	38.9
0.02°	2^{18}	3.765	100.0	39.8
0.05°	2^{16}	2.298	100.0	69.0
0.05°	2^{18}	3.500	92.5	44.3
0.10°	2^{16}	2.122	92.1	72.3
0.10°	2^{18}	2.715	48.7	59.0

4.7 Link Stability Under Pointing Errors

Table 8 and Figs. 8–9 quantify link stability when the stochastic pointing model of Section 3.8 replaces the fixed 1 dB penalty (the $\sigma = 0$ rows are the ideal-pointing baseline on the same budget). Two regimes emerge. For $\sigma \leq 0.02°$, all array sizes remain fully aligned and the ensemble-mean spectral efficiency at $N = 2^{18}$ is within 0.06 bps/Hz of ideal. At $\sigma = 0.05°$ the largest array begins to lose alignment (92.5%), and at $\sigma = 0.10°$ alignment at $N = 2^{18}$ collapses to 48.7% while mean spectral efficiency falls from 3.82 to 2.72 bps/Hz and outage ($\eta_{SE} < 3\,\text{bps/Hz}$) rises from 38.9% to 59.0%. Because the beam narrows as $N^{-1/2}$ while aperture gain grows by 3.01 dB per doubling, the expected pointing loss grows in proportion to $N\sigma^2$; equating the marginal loss to the marginal gain places the jitter-limited optimum near $N^\star \approx 3.01 \cdot (2.04)^2/(24\sigma^2_{\text{rad}})$, i.e. about $2^{17.4}$ at $\sigma = 0.10°$, at the upper edge of the sampled range, where the Monte Carlo means at 2^{17} and 2^{18} are already nearly indistinguishable. Under jitter beyond $\approx 0.1°$, further aperture enlargement is counterproductive, and the sizing rule of Section 5 must be read jointly with the achievable tracking accuracy.

4.8 Pass-Level Performance

Figure 10 shows spectral efficiency over an overhead $h_s = 800\,\text{km}$ pass at $\sigma = 0.02°$ for three array sizes, with the elevation profile overlaid. The channel is dynamic but slowly varying on the beam-update timescale: spectral efficiency tracks the slant-range profile, peaking at closest approach, and the required phase-update rate (tens of Hz, Section 3.9) is three or more orders of magnitude below demonstrated RIS reconfiguration speeds [45, 46].

4.9 Sensitivity to Deformation, Ephemeris Quality, and Latency

Figures 11–13 quantify the budgets of Section 3.10 on the full ensemble, holding the pointing jitter at the benign level $\sigma = 0.02°$ so that each new mechanism is isolated. Surface deformation is the strongest of the three: sweeping δ from 0 to 100 μm lowers ensemble-mean spectral efficiency from 1.64 to 1.04 bps/Hz, and the loss accelerates with frequency through (14), which is why the

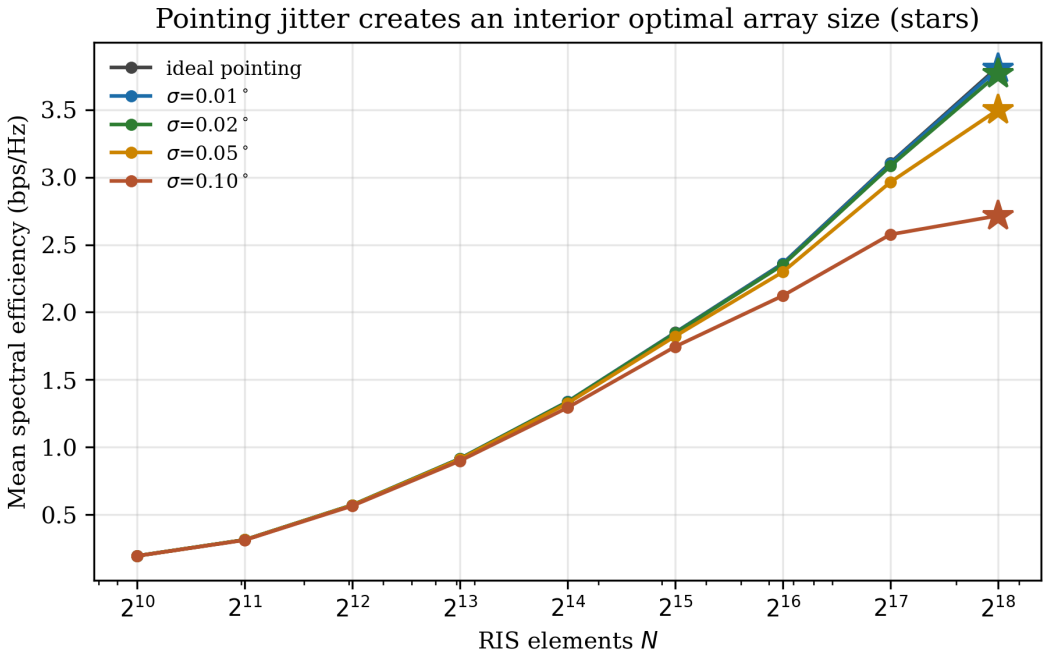


Figure 8: Ensemble-mean spectral efficiency versus N under pointing jitter. Gains flatten and then erode as jitter consumes the narrowing beam.

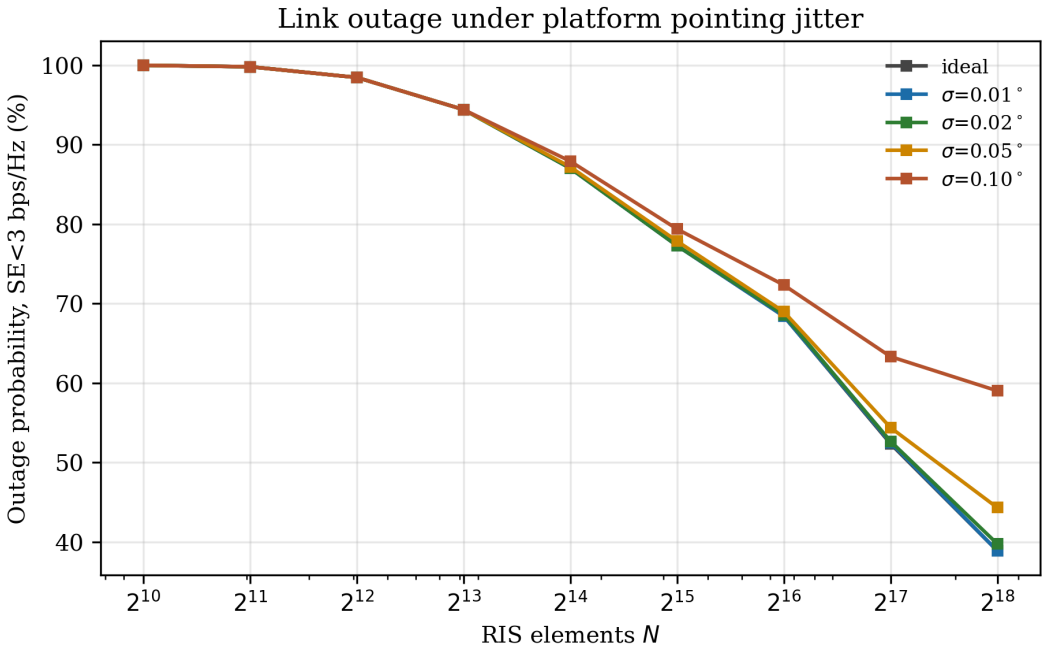


Figure 9: Outage probability ($\eta_{SE} < 3$ bps/Hz) versus N and jitter level.

micrometre-class tolerances above are stated as requirements. Control latency is benign against orbital motion: staleness contributes negligibly up to 20 ms and costs only 0.08 bps/Hz of mean

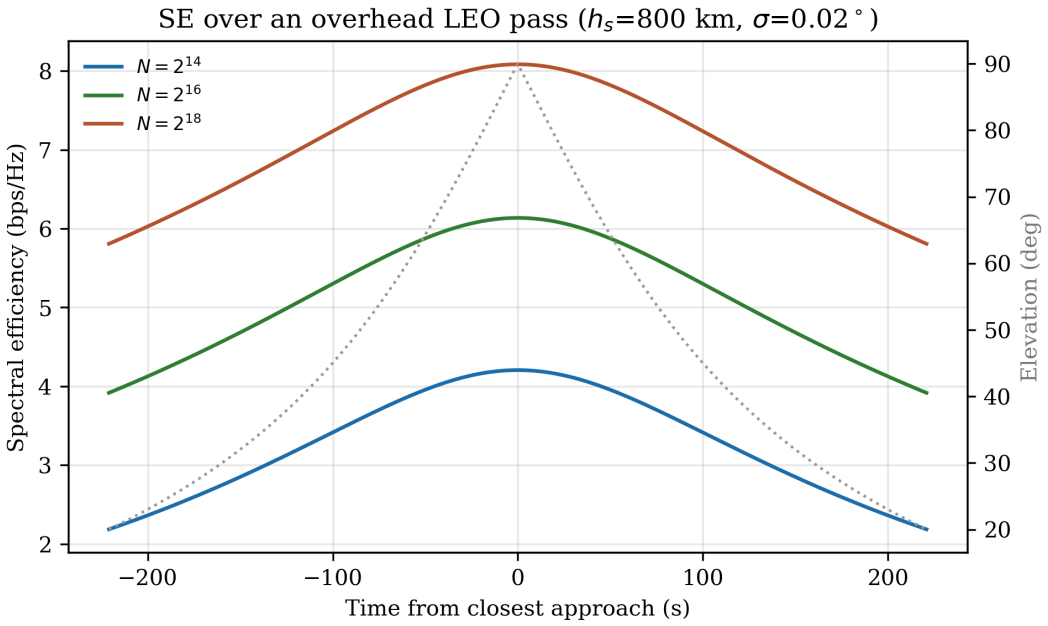


Figure 10: Spectral efficiency over an overhead LEO pass ($h_s = 800\,\text{km}$, $h_p = 16\,\text{km}$, $\sigma = 0.02°$); dotted curve: elevation angle.

spectral efficiency at 100 ms. Ephemeris error is negligible at GNSS grade but material at two-line-element grade for the largest arrays: with a 1 km position error the $N = 2^{18}$ subset falls from 3.76 to 3.34 bps/Hz in mean spectral efficiency and from 100% to 87.7% alignment, while arrays of $N \leq 2^{14}$, whose beams are wider than 0.9°, are essentially insensitive. Sensitivity to channel-estimation error is the σ sweep of Section 4.7 itself, since estimation residuals enter the pointing model only through σ; together with the three axes here and the Doppler budget, the four dynamic-channel sensitivities (estimation error, positional uncertainty, Doppler, and latency) are each quantified. Doppler (Fig. 12) remains a carrier-recovery task rather than a beamforming constraint. Taken together with Section 4.7, the quantified feasibility conditions for the proposed system are micrometre-class panel stability, precise orbit data beyond $N = 2^{16}$, residual tracking jitter below about 0.05°, and control latency below a few tens of milliseconds, each of which is individually within demonstrated engineering practice.

5 Discussion

The results show that the performance of the hybrid RIS-assisted air-to-satellite terahertz (THz) system is governed jointly by communication, propagation, and geometric parameters, with a clear ordering of influence. RIS array size is the strongest positive predictor of performance ($\beta = +0.734$ on the SNR scale), followed by transmit power ($\beta = +0.538$); carrier frequency is the strongest negative predictor ($\beta = -0.319$), followed by slant range ($\beta = -0.272$). The negative frequency

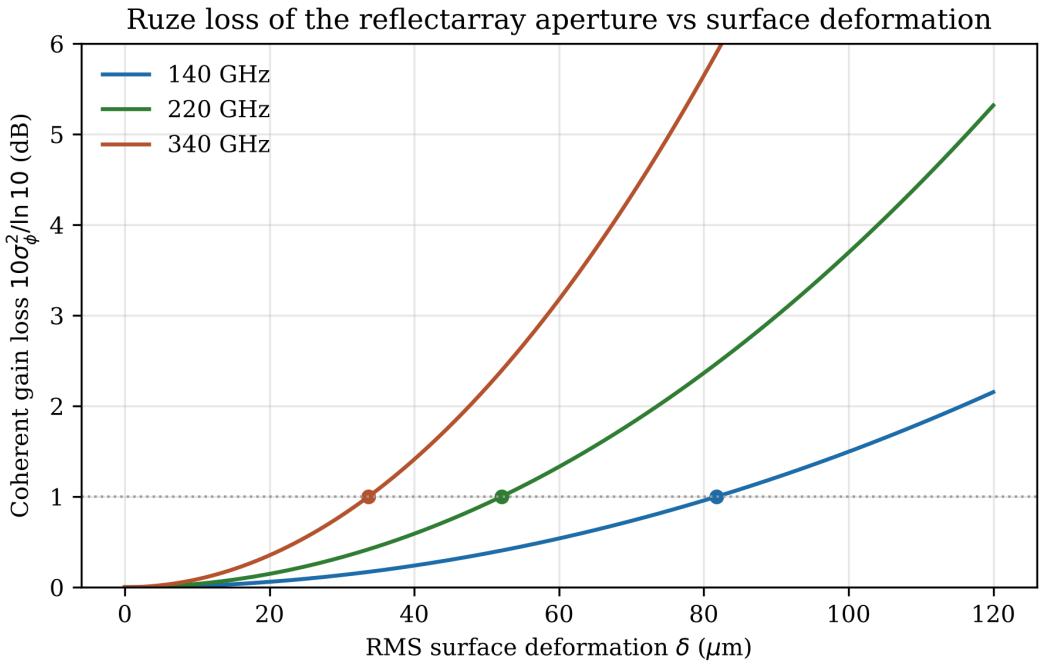


Figure 11: Ruze gain loss of the reflectarray aperture versus RMS surface deformation; markers show the 1 dB tolerance at each frequency.

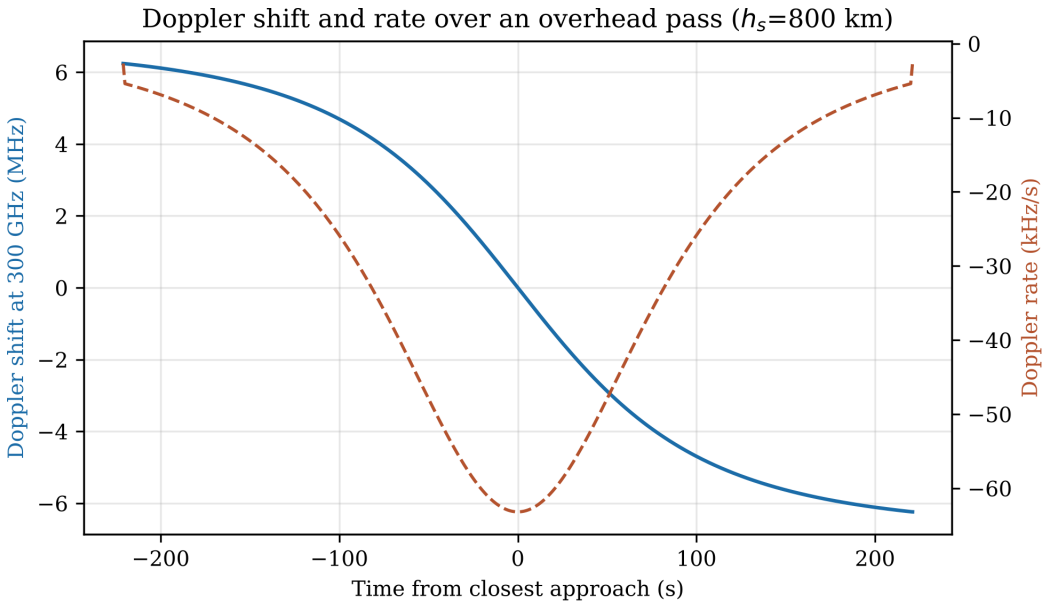


Figure 12: Doppler shift (solid) and Doppler rate (dashed) at 300 GHz over the overhead reference pass.

effect is consistent with the known propagation properties of THz channels [21, 39]. However, the altitude-resolved absorption model refines the interpretation of this effect: within the transmission windows, and for platforms at or above 8 km, the frequency penalty is carried almost entirely by

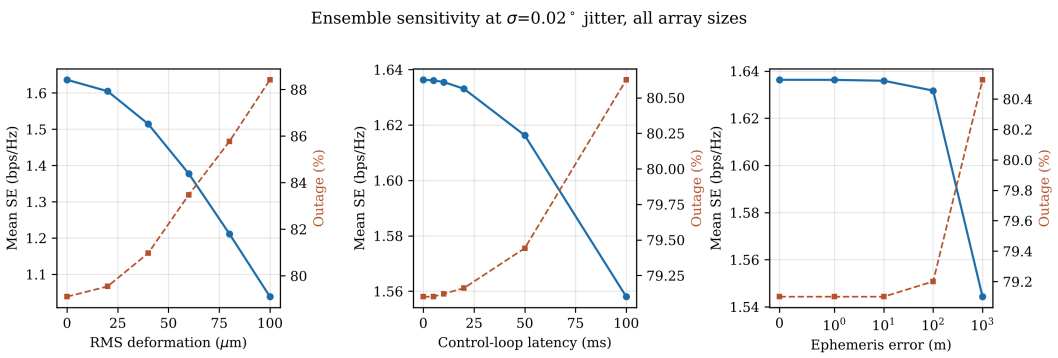


Figure 13: Ensemble sensitivity of mean spectral efficiency (solid, left axes) and outage (dashed, right axes) to surface deformation, control-loop latency, and ephemeris error at $\sigma = 0.02°$.

free-space spreading rather than by molecular absorption, whose correlation with SNR is small ($r = -.08$).

This altitude finding merits emphasis, as, to the best of the authors' knowledge, it has received relatively little attention in prior statistical treatments of RIS-assisted non-terrestrial links. Ground-anchored analyses (e.g., [9]) correctly identify water-vapour absorption as a first-order constraint on Earth-satellite THz feasibility and motivate careful window selection. The layered ITU-R P.676-12/P.835 integration used here shows that this constraint largely dissolves for high-altitude platforms: the 183 and 325 GHz water-vapour lines, which dominate the ground-level spectrum, weaken by more than an order of magnitude at 8 km and by roughly two orders at 12 km (Fig. 2), and zenith absorption at the 140, 220, and 340 GHz window centres falls to at most 0.2 dB at 8 km and below 0.05 dB at 12 km (Table 1). Consequently, platform altitude (previously reported as a non-significant factor in surface-anchored analyses) carries a small but reliable positive effect once absorption is evaluated from the platform upward, and the binding constraints on high-altitude THz link design shift from the atmosphere to aperture and spreading loss. This observation is consistent with, and extends, the airplane-to-satellite channel modeling of Kokkoniemi *et al.* [22], which likewise found favorable propagation for airborne THz links under suitable operating conditions.

The dominance of RIS configuration indicates that the severe spreading loss of THz communication is most effectively countered by enlarging the coherently phased aperture. The mechanism is the explicit chain of (11): each doubling of N adds 3.01 dB of aperture gain, which translates to approximately one additional bit/s/Hz in the high-SNR regime but to progressively less below 0 dB SNR. Two design consequences follow. First, the quantitative sizing rule: for the reference geometry, mean SNR crosses zero between 2^{15} and 2^{16} elements, and sustained spectral efficiencies above 3 bps/Hz over ∼1000 km require arrays of the order of 10^4–10^5 elements: physically modest panels of 9-35 cm per side at 220 GHz, compatible in *footprint* with conformal mounting on an airborne platform. Published hardware anchors this feasibility assessment: demonstrated prototypes include a 256-element 2-bit PIN-diode surface at 2.3/28.5 GHz [44], an 1100-element surface at 5.8 GHz con-

suming about 1 W in total [45], and a 2430-element varactor surface at 3.5 GHz [46]. Linear scaling of the measured control power of [45] suggests order-of-100 W-class control budgets for 10^5 PIN-switched elements, with varactor biasing substantially lower; no flight-qualified terahertz surface at 10^4–10^5 elements has been demonstrated to date, and the cited prototypes operate at microwave frequencies on static mounts; airborne integration has so far been treated at the design level, where UAV payload and battery limits are identified as the binding constraint on element count [48]. On payload mass, flight-qualified reflectarray hardware provides a direct anchor: the ISARA mission flew a three-panel $33.4 \times 26.8\,\mathrm{cm}^2$ Ka-band reflectarray, essentially the panel scale of $N = 2^{18}$ at 220 GHz, at a total antenna mass of 0.5 kg including feed and integrated solar array [47], so the aperture itself is a sub-kilogram payload well within the tens-of-kilogram capacities of the tethered and high-altitude platforms surveyed in [42]; the mass, power, and complexity burden of 10^4–10^5 phase-control channels, not the panel, is the open engineering problem. This footprint argument should not be mistaken for a claim of easy realizability. The same panels carry 10^4 to 2.6×10^5 individually phase-controlled elements at $\lambda/2 \approx 0.68$ mm pitch; a 512×512 controllable reflectarray at 220 GHz is a demanding fabrication, biasing, and real-time control problem irrespective of its modest size, and the beam it forms (0.23° at $N = 2^{18}$) must be steered and stabilised against platform motion and satellite transit. The result should thus be read as establishing that aperture, not atmosphere or raw panel area, is the binding constraint-while the element count and its control remain the principal open engineering challenge. Second, the diminishing-returns regime implies that under-provisioned arrays cannot be rescued by transmit power alone: although transmit power carries a substantial coefficient, its 20 dB sampled range contributes less headroom than the 24 dB spanned by the array sizes considered, and neither compensates for operating far below the SNR transition. These findings are consistent with the theoretical aperture treatments of Özdogan *et al.* [49] and Björnson and Sanguinetti [27], and with reports that passive beamforming optimization yields substantial spectral-efficiency gains [18, 29]. The present contribution is to place these effects in a single statistical ranking under a fully specified, altitude-resolved propagation model.

The effects of slant range and elevation angle highlight the role of transmission geometry. Longer slant ranges increase spreading loss and reduce spectral efficiency; higher elevation angles shorten the path, and their influence in the regression is carried by the slant-range term with which elevation is strongly collinear ($r = -.68$). Under the altitude-resolved model this geometric effect operates through free-space loss rather than through cumulative atmospheric attenuation, a mechanistic distinction from ground-anchored links, where the elevation effect compounds both. This is in line with the channel-modeling results of Kokkoniemi *et al.* [22] and with the space-air-ground analyses of Zhang *et al.* [40], while clarifying the mechanism for the high-altitude regime.

Methodologically, the present study differs from prior performance evaluations in three respects. First, the channel model is stated in full (Eqs. (1)-(10)) with a worked link budget (Table 2), and the entire analysis is regenerated by a fixed-seed pipeline, so all results are reproducible from the

equations alone. Second, primary statistical inference is conducted on the SNR scale, which is uncensored and linear in the decibel-domain design terms, avoiding the bias that the spectral-efficiency floor at zero induces in least-squares estimation; the companion spectral-efficiency model preserves the same ordering of effects. Third, definitional relationships (such as the SNR–spectral-efficiency correlation) are reported but explicitly excluded from interpretation, and, given the deterministic simulation design, significance levels are read as sensitivity indices over the operating envelope rather than as population inference. Prior studies have typically evaluated individual metrics or specific optimization scenarios: outage and capacity under varying RIS configurations [37], BER via Monte Carlo simulation [38], analytical capacity under atmospheric impairments [39], and secrecy performance under turbulence, pointing errors, and imperfect CSI [35]. The complementary contribution here is a transparent, model-grounded ranking of the dominant design variables within the viable operating envelope.

Practically, the results yield four design implications for RIS-assisted air-to-satellite THz systems. First, for high-altitude platforms, carrier selection within the 100-420 GHz range is constrained less by atmospheric windows than by the free-space frequency penalty; avoiding only the narrow line cores at 183 and 325 GHz suffices, and the traditional ground-level window map is overly conservative above 8 km. Second, RIS provisioning is the principal lever on performance within the sampled envelope, with a concrete sizing rule of 3 dB per doubling and a viability transition near $10^{4.5}$ elements for $\sim$1000 km links; the required element count, rather than the panel area, is what makes this lever costly to pull, and the gains quoted for the largest arrays presume beam tracking that holds the sub-degree beam and an illumination efficiency that a full near-field model would reduce. Third, favorable geometry (higher elevation and shorter slant range) remains valuable, operating through spreading loss. Fourth, transmit power is a meaningful but secondary lever *over the ranges sampled here*, and cannot substitute for adequate aperture. Together these findings support propagation-aware, aperture-first design of THz non-terrestrial links, subject to the pointing, hardware, and near-field caveats above.

6 Conclusion

This study examined the spectral efficiency of hybrid reconfigurable intelligent surface (RIS)-assisted air-to-satellite terahertz (THz) communication systems, in which an active airborne feed illuminates a co-located passive RIS reflectarray directed at a low-Earth-orbit satellite. A fully specified physics-based channel model (combining Friis free-space loss, an RIS aperture gain of $10\log_{10}(\pi\eta_a N)$, altitude-resolved ITU-R P.676-12/P.835 gaseous absorption integrated from the platform upward, and explicit reflection, pointing, and polarization losses) was used to generate 5,000 links, which were analysed by descriptive statistics, correlation analysis, and heteroscedasticity-robust regression with primary inference on the uncensored SNR scale.

The results show that RIS array size is the strongest positive determinant of performance ($\beta = +0.734$), followed by transmit power, while carrier frequency is the strongest negative determinant ($\beta = -0.319$), followed by slant range. Above approximately 8 km platform altitude, gaseous absorption within the transmission windows becomes negligible, so the frequency penalty is driven by free-space spreading and the binding design constraints shift from the atmosphere to aperture and geometry; platform altitude itself carries a small but reliable positive effect. Mean SNR crosses zero between 2^{15} and 2^{16} RIS elements for the reference geometry, and spectral efficiencies above 3 bps/Hz over $\sim$1000 km require arrays of the order of 10^4–10^5 elements: panels of only 9–35 cm per side at 220 GHz. These results provide quantitative, reproducible guidance for the joint selection of carrier frequency, RIS aperture, and link geometry in future 6G non-terrestrial networks.

Several idealizations bound the scope of these results and should temper the practicality of the largest apertures in particular. The analysis was carried out on deterministic channels with idealized coherent RIS beamforming: small-scale fading, atmospheric turbulence, and THz phase noise and hardware impairments, which are first-order effects at these frequencies, were not modeled. The pointing penalty was fixed at 1 dB, whereas the coherent beam narrows to a few tenths of a degree for the largest arrays and would in practice require closed-loop tracking of a fast-moving LEO target from a moving platform, whose residual jitter is the operationally binding term; the stability analysis of Section IV-G quantifies this regime, and jitter beyond about 0.1° makes further aperture enlargement counterproductive. The phase-coherence, ephemeris, Doppler, and latency budgets of Sections III-J and IV-I translate the remaining dynamic-channel concerns into verifiable engineering requirements: micrometre-class surface stability, precise orbit knowledge for arrays beyond 2^{16} elements, and a control loop no slower than a few tens of milliseconds. The aperture efficiency was held constant, although the few-metre feed standoff places the largest arrays in their near field, where a full illumination model would reduce the effective gain. The reported gains also assume a 500 K system noise temperature, optimistic for an uncooled THz receiver, with every 3 dB of additional noise equivalent to removing one doubling of N. Finally, the 10^4–10^5 element counts implied by the sizing rule, while modest in panel area, represent a substantial fabrication and real-time control challenge. Reported significance levels index sensitivity within the simulated design space rather than population inference. Future research may incorporate realistic RIS hardware and near-field illumination constraints, beam-tracking jitter, stochastic fading and turbulence models, and validation through experimental measurements or actual air-to-satellite communication datasets to further strengthen the framework's practical applicability.

List of abbreviations

6G Sixth generation (of wireless networks)

CSI Channel state information

FSPL Free-space path loss

GNSS Global navigation satellite system

HC3 Heteroscedasticity-consistent covariance estimator (type 3)

ITU-R International Telecommunication Union, Radiocommunication Sector

LEO Low Earth orbit

OLS Ordinary least squares

PIN Positive-intrinsic-negative (diode)

RIS Reconfigurable intelligent surface

RMS Root mean square

SE Spectral efficiency

SNR Signal-to-noise ratio

THz Terahertz

TLE Two-line element (ephemeris)

UAV Unmanned aerial vehicle

VIF Variance inflation factor

Declarations

Availability of data and materials

The simulation dataset generated and analysed during the current study, together with the fixed-seed code that regenerates every table and figure, is available from the corresponding author on reasonable request.

Competing interests

The authors declare that they have no competing interests.

Funding

This work was funded by the Deanship of Research and Graduate Studies at King Khalid University through the Large Group Project under grant number RGP.2/265/46.

Authors' contributions

M.A. developed the study concept, carried out the simulations and analysis, and drafted the manuscript. I.K. supervised the methodology and reviewed the channel model. M.M.A. reviewed the statistical analysis and the manuscript. All authors read and approved the final manuscript.

Acknowledgements

The authors extend their appreciation to the Deanship of Research and Graduate Studies at King Khalid University for funding this work through the Large Group Project under grant number RGP.2/265/46.

References

[1] Muhammad Sohail Akbar, Zawar Hussain, Muhammad Ikram, Quan Z. Sheng, and Subhas C. Mukhopadhyay. On challenges of sixth-generation (6G) wireless networks: A comprehensive survey of requirements, applications, and security issues. *Journal of Network and Computer Applications*, 233:104040, 2025.

[2] Stefanos Plastras, Dimitrios Tsoumatidis, Dimitrios N. Skoutas, Angelos Rouskas, Georgios Kormentzas, and Charalabos Skianis. Non-terrestrial networks for energy-efficient connectivity of remote IoT devices in the 6G era: A survey. *Sensors*, 24(4):1227, 2024.

[3] Wei Jiang, Qiuheng Zhou, Jiguang He, Mohammad Asif Habibi, Sergiy Melnyk, Mohammed El-Absi, Bin Han, Marco Di Renzo, Hans D. Schotten, and Fa-Long Luo. Terahertz communications and sensing for 6G and beyond: A comprehensive review. *IEEE Communications Surveys & Tutorials*, 26(4):2326–2381, 2024.

[4] Saeed Sharif, Sherali Zeadally, and Waleed Ejaz. Space-aerial-ground-sea integrated networks: Resource optimization and challenges in 6G. *Journal of Network and Computer Applications*, 215:103647, 2023.

[5] Yue Xiao, Zhi Ye, Min Wu, Hang Li, Ming Xiao, Mohamed-Slim Alouini, Akram Al-Hourani, and Stefano Cioni. Space-air-ground integrated wireless networks for 6G: Basics, key technologies, and future trends. *IEEE Journal on Selected Areas in Communications*, 42(12):3327–3354, 2024.

[6] Jianjun Ma, Yi Song, Mingxia Zhang, Guohao Liu, Wei Li, John F. Federici, and Daniel M. Mittleman. Terahertz channels in atmospheric conditions: Propagation characteristics and security performance. *Fundamental Research*, 5(2):526–555, 2025.

[7] Fahd Taleb, Marcos Alfaro-Gomez, Mohammed D. Al-Dabbagh, Jan Ornik, João Viana, Anselm Jäckel, Christian Mach, Jacob Helminiak, Thomas Kleine-Ostman, Thomas Kürner, Martin Koch, Daniel M. Mittleman, and Enrique Castro-Camus. Propagation of THz radiation in air over a broad range of atmospheric temperature and humidity conditions. *Scientific Reports*, 13(1):20782, 2023.

[8] Masoud Taherkhani, Zahra Ghassemlooy Kashani, and Ramezan Ali Sadeghzadeh. On the performance of THz wireless LOS links through random turbulence channels. *Nano Communication Networks*, 23:100282, 2020.

[9] Muhammad Saqlain, Nasir M. Idrees, Shu Wang, and Xianbin Yu. Channel modeling and performance analysis of fixed terahertz Earth-satellite links in the low- and mid-latitude regions. *Optical Engineering*, 60(3):036103, 2021.

[10] Sadiq Sualiheen, Chaitali J. Pawase, and KyungHi Chang. Link budget analysis for dual-steering based ground-to-air and satellite-to-air communications in 6G networks. *IEEE Access*, 2025.

[11] Ertugrul Basar, Marco Di Renzo, Julien De Rosny, Mérouane Debbah, Mohamed-Slim Alouini, and Rui Zhang. Wireless communications through reconfigurable intelligent surfaces. *IEEE Access*, 7:116753–116773, 2019.

[12] Bo Wang, Yi Zhang, Fei Chu, Guoru Ding, and Ruoyu Xu. Analysis and optimization of UAV-assisted covert communications in interweave cognitive radio networks. *IEEE Transactions on Cognitive Communications and Networking*, 11(5):3188–3201, 2025.

[13] Qingqing Wu, Beixiong Zheng, Changsheng You, Lipeng Zhu, Kaiming Shen, Xiaodan Shao, Weidong Mei, Boya Di, Hongliang Zhang, and Ertugrul Basar. Intelligent surfaces empowered wireless network: Recent advances and the road to 6G. *Proceedings of the IEEE*, 112(7): 724–763, 2024.

[14] Francesco Alessio Dicandia, Nelson J. Fonseca, Manlio Bacco, Simone Mugnaini, and Simone Genovesi. Space-air-ground integrated 6G wireless communication networks: A review of antenna technologies and application scenarios. *Sensors*, 22(9):3136, 2022.

[15] Jianjun Ma, Peian Li, and Wenbo Liu. *Terahertz channel measurement, modeling, and security properties: Fundamentals, techniques, and applications*. CRC Press, 2025.

[16] Marco Di Renzo, Alessio Zappone, Mérouane Debbah, Mohamed-Slim Alouini, Chau Yuen, Julien De Rosny, and Sergei Tretyakov. Smart radio environments empowered by reconfigurable intelligent surfaces: How it works, state of research, and the road ahead. *IEEE Journal on Selected Areas in Communications*, 38(11):2450–2525, 2020.

[17] Feibo Jiang, Cunhua Pan, Li Dong, Kezhi Wang, Mérouane Debbah, Dusit Niyato, and Zhu Han. A comprehensive survey of large AI models for future communications: Foundations, applications and challenges. *IEEE Communications Surveys & Tutorials*, 2026.

[18] Chongwen Huang, Zhaohui Yang, George C. Alexandropoulos, Kezhi Xiong, Li Wei, Chau Yuen, Zhaoyang Zhang, and Mérouane Debbah. Multi-hop RIS-empowered terahertz communications: A DRL-based hybrid beamforming design. *IEEE Journal on Selected Areas in Communications*, 39(6):1663–1677, 2021.

[19] Christian E. Worka, Fasih A. Khan, Qasim Z. Ahmed, Pradorn Sureephong, and Temitope Alade. Reconfigurable intelligent surface (RIS)-assisted non-terrestrial network (NTN)-based 6G communications: A contemporary survey. *Sensors*, 24(21):6958, 2024.

[20] Wenhao Chen, Lu Li, Zhi Chen, and Tony Q. Quek. Coverage modeling and analysis for outdoor THz networks with blockage and molecular absorption. *IEEE Wireless Communications Letters*, 10(5):1028–1031, 2021.

[21] Rafael Vieira Da Nóbrega, Thiago R. Raddo, Antonio Jurado-Navas, Murilo B. Loiola, Anderson L. Sanches, and Mérouane Debbah. A channel loss model for THz networks from 100–600 GHz considering both molecular and water vapor continuum absorptions. *IEEE Open Journal of Vehicular Technology*, 4:475–489, 2023.

[22] Joonas Kokkoniemi, Josep M. Jornet, Vitaly Petrov, Yevgeni Koucheryavy, and Markku Juntti. Channel modeling and performance analysis of airplane-satellite terahertz band communications. *IEEE Transactions on Vehicular Technology*, 70(3):2047–2061, 2021.

[23] Shuai Nie and Ian F. Akyildiz. Channel modeling and analysis of inter-small-satellite links in terahertz band space networks. *IEEE Transactions on Communications*, 69(12):8585–8599, 2021.

[24] Jie Yang, Hao Li, and Zhen Xu. Analysis of channel characteristics between satellite and space station in terahertz band based on ray tracing. *Radio Science*, 56(9):1–16, 2021.

[25] Wesam M. Othman, Abdelhamied A. Ateya, Mohammed E. Nasr, Ammar Muthanna, Mohammed ElAffendi, Andrey Koucheryavy, and Amr A. Hamdi. Key enabling technologies for 6G: The role of UAVs, terahertz communication, and intelligent reconfigurable surfaces in shaping the future of wireless networks. *Journal of Sensor and Actuator Networks*, 14(2):30, 2025.

[26] Mohammed Almekhlafi, Mohamed Amine Arfaoui, Chadi Assi, and Ali Ghrayeb. A low-complexity passive beamforming design for reconfigurable intelligent surface (RIS) in 6G networks. *IEEE Transactions on Vehicular Technology*, 72(5):6309–6321, 2023.

[27] Emil Björnson and Luca Sanguinetti. Rayleigh fading modeling and channel hardening for reconfigurable intelligent surfaces. *IEEE Wireless Communications Letters*, 10(4):830–834, 2020.

[28] Manzoor Ahmed, Abdul Wahid, Wali Ullah Khan, Feroz Khan, Asim Ihsan, Zain Ali, Khaled M. Rabie, Thokozani Shongwe, and Zhu Han. A survey on RIS advances in terahertz communications: Emerging paradigms and research frontiers. *IEEE Access*, 12:173867–173901, 2024.

[29] Ming-Min Zhao, Qingqing Wu, Min-Jian Zhao, and Rui Zhang. Intelligent reflecting surface enhanced wireless networks: Two-timescale beamforming optimization. *IEEE Transactions on Wireless Communications*, 20(1):2–17, 2020.

[30] Yali Chen, Bo Ai, Hongliang Zhang, Yong Niu, Lingyang Song, Zhu Han, and H. Vincent Poor. Reconfigurable intelligent surface assisted device-to-device communications. *IEEE Transactions on Wireless Communications*, 20(5):2792–2804, 2020.

[31] Muhammad Tariq, Sohail Ahmad, Mian Ahmad Jan, and Houbing Song. Deep learning aided intelligent reflective surfaces for 6G: A survey. *ACM Computing Surveys*, 57(3):63, 2024.

[32] Yue Yin, Long Yang, Xingwang Li, Hongwu Liu, Kefeng Guo, and Yun Li. On the performance of active RIS-assisted mixed RF-THz relaying systems. *IEEE Internet of Things Journal*, 12 (10):14938–14951, 2025.

[33] Wan Yi Dong, Shuo Yang, Ping Zhang, and Sheng Chen. Modeling and performance analysis of IoT-over-LEO satellite systems under realistic operational constraints: A stochastic geometry approach. *IEEE Internet of Things Journal*, 12(15):30576–30593, 2025.

[34] Kazuki Tamesue, Suthee H. Myint, Kaito Jitsuno, Takuro Sato, Takashi Sato, and Tetsuya Kawanishi. Scheme design for high-throughput terahertz feeder link in non-terrestrial networks. *Journal of Advanced Simulation in Science and Engineering*, 11(1):1–11, 2024.

[35] Jiankang Yuan, Gaojie Chen, Miaowen Wen, Rahim Tafazolli, and Erdal Panayirci. Secure transmission for THz-empowered RIS-assisted non-terrestrial networks. *IEEE Transactions on Vehicular Technology*, 72(5):5989–6000, 2023.

[36] Ebrahim E. Elsayed, Mohammed R. Hayal, Iskandar Nurhidayat, Mohd Adnan Shah, Amir Elfikky, Ahmed I. Boghdady, Davron A. Juraev, and Mohamed A. Morsy. Coding techniques for diversity enhancement of dense wavelength division multiplexing MIMO-FSO fault protection protocols systems over atmospheric turbulence channels. *IET Optoelectronics*, 18(1–2):11–31, 2024.

[37] Tianwei Hou and Anna Li. Performance analysis of NOMA-RIS aided integrated navigation and communication (INAC) networks. *IEEE Transactions on Vehicular Technology*, 72(10): 13255–13268, 2023.

[38] Yan Wang, Hui Wang, and Xiaowen Jiang. Performance of reconfigurable-intelligent-surface-assisted satellite quasi-stationary aircraft–terrestrial laser communication system. *Drones*, 6 (12):405, 2022.

[39] George K. Varotsos, Konstantinos Aidinis, Athanassios Katsis, and Hector E. Nistazakis. Capacity performance analysis for terrestrial THz channels. *Electronics*, 12(6):1336, 2023.

[40] Chao Zhang, Qiang Li, Chen Xu, Lie-Liang Yang, and Lajos Hanzo. Space-air-ground integrated networks: Their channel model and performance analysis. *IEEE Open Journal of Vehicular Technology*, 6:1501–1523, 2025.

[41] Yishi Zhu, Bomin Mao, and Nei Kato. Intelligent reflecting surface in 6G vehicular communications: A survey. *IEEE Open Journal of Vehicular Technology*, 3:266–277, 2022.

[42] Baha Eddine Youcef Belmekki and Mohamed-Slim Alouini. Unleashing the potential of networked tethered flying platforms: Prospects, challenges, and applications. *IEEE Open Journal of Vehicular Technology*, 3:278–320, 2022.

[43] Mohammed Almekhlafi, Antoine Lesage-Landry, and Güneş Karabulut Kurt. Access inequality in LEO satellite networks: A case study of high-latitude coverage in northern Québec. *IEEE Open Journal of Vehicular Technology*, 6:1613–1630, 2025.

[44] Linglong Dai, Bichai Wang, Min Wang, Xue Yang, Jingbo Tan, Shuangkaisheng Bi, Shenheng Xu, Fan Yang, Zhi Chen, Marco Di Renzo, Chan-Byoung Chae, and Lajos Hanzo. Reconfigurable intelligent surface-based wireless communications: Antenna design, prototyping, and experimental results. *IEEE Access*, 8:45913–45923, 2020.

[45] Xilong Pei, Haifan Yin, Li Tan, Lin Cao, Zhanpeng Li, Kai Wang, Kun Zhang, and Emil Björnson. RIS-aided wireless communications: Prototyping, adaptive beamforming, and indoor/outdoor field trials. *IEEE Transactions on Communications*, 69(12):8627–8640, 2021.

[46] Ali Araghi, Mohsen Khalily, Mahmood Safaei, Amirmasood Bagheri, Vikrant Singh, Fan Wang, and Rahim Tafazolli. Reconfigurable intelligent surface (RIS) in the sub-6 GHz band: Design, implementation, and real-world demonstration. *IEEE Access*, 10:2646–2655, 2022.

[47] Richard E. Hodges, Dorothy K. Lewis, Matthew J. Radway, Armen S. Toorian, Fernando H. Aguirre, Daniel J. Hoppe, Biren N. Shah, and Andrew A. Gray. The ISARA mission – flight demonstration of a high gain Ka-band antenna for 100 Mbps telecom. In *Proc. AIAA/USU Conf. Small Satellites*, 2018.

[48] Bodong Shang, Rubayet Shafin, and Lingjia Liu. UAV swarm-enabled aerial reconfigurable intelligent surface. *IEEE Wireless Communications*, 2021.

[49] Özgecan Özdogan, Emil Björnson, and Erik G. Larsson. Intelligent reflecting surfaces: Physics, propagation, and pathloss modeling. *IEEE Wireless Communications Letters*, 9(5):581–585, 2020.